ELSEVIER

Medical Image Analysis 6 (2002) 109–128

MEDICAL IMAGE ANALYSIS

www.elsevier.com/locate/media

Fusing speed and phase information for vascular segmentation of phase contrast MR angiograms

Albert C.S. Chung[a], J. Alison Noble[a,*], Paul Summers[b]

[a]*Medical Vision Laboratory, Department of Engineering Science, Oxford University, OX1 3PJ, Oxford, UK*
[b]*Department of Clinical Neuroscience, King's College London, London, UK*

Received 4 January 2001; received in revised form 10 July 2001; accepted 26 October 2001

Abstract

This paper presents a statistical approach to aggregating speed and phase (directional) information for vascular segmentation of phase contrast magnetic resonance angiograms (PC-MRA). Rather than relying on speed information alone, as done by others and in our own work, we demonstrate that including phase information as a priori knowledge in a Markov random field (MRF) model can improve the quality of segmentation. This is particularly true in the region within an aneurysm where there is a heterogeneous intensity pattern and significant vascular signal loss. We propose to use a Maxwell–Gaussian mixture density to model the background signal distribution and combine this with a uniform distribution for modelling vascular signal to give a Maxwell–Gaussian-uniform (MGU) mixture model of image intensity. The MGU model parameters are estimated by the modified expectation-maximisation (EM) algorithm. In addition, it is shown that the Maxwell–Gaussian mixture distribution (a) models the background signal more accurately than a Maxwell distribution, (b) exhibits a better fit to clinical data and (c) gives fewer false positive voxels (misclassified vessel voxels) in segmentation. The new segmentation algorithm is tested on an aneurysm phantom data set and two clinical data sets. The experimental results show that the proposed method can provide a better quality of segmentation when both speed and phase information are utilised.

Keywords: Magnetic resonance angiography (MRA); Expectation-maximisation (EM) algorithm; Markov random fields (MRF); Flow coherence; MR signal modelling and statistical segmentation

1. Introduction

Magnetic resonance angiography (MRA) is a collection of non-invasive methods for vessel delineation. Three major groups of MRA techniques are time-of-flight (TOF) MRA, contrast enhanced (CE) MRA and phase contrast (PC) MRA. The main advantage of PC-MRA over TOF- and CE-MRA is that it not only gives information about vascular morphology but also provides for each voxel a three-component estimate of flow direction (in the form of phase images) and rate of flow (conveyed as a speed image). Moreover, a PC-MRA speed image has good background suppression and displays two high contrast voxel types: vessel and background (Rinck, 1993). Medical diagnosis of vascular diseases is commonly performed on the basis of an analysis of MRA speed images alone, which assign high intensity to the moving blood and cerebrospinal fluid (CSF). The work described in this paper was entirely driven by the growing need of PC-MRA image segmentation for characterisations of vasculature and aneurysms.

While most of the arterial anatomy can be shown clearly in MRA speed images, this is not the case for, for example, intracranial aneurysms. These can contain low or complex flow and are poorly represented in the images (Steiger et al., 1997; Wilcock et al., 1995). The presence of an aneurysm causes significant vascular signal loss in the MRA speed image with some intensity levels approximately equal to those of background signal, thereby producing a

*Corresponding author. Tel.: +44-1865-280-934; fax: +44-1865-280-922.
E-mail address: noble@robots.ox.ac.uk (J.A. Noble).

1361-8415/02/$ – see front matter
PII: S1361-8415(02)00057-9

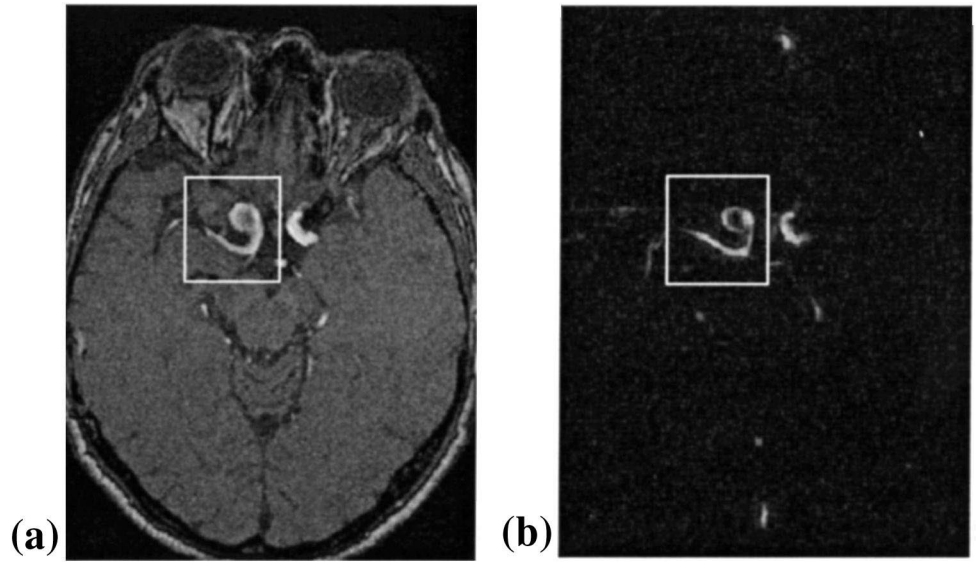

Fig. 1. (a) Time-of-flight (TOF) MRA; (b) phase contrast (PC) MRA. As shown in the figures, the presence of an aneurysm causes significant vascular signal loss in the MRA speed image with some intensity levels approximately equal to those of background signal, thereby producing a heterogeneous intensity pattern within the aneurysm. The inclusion of such regions of inhomogeneous intensities is a challenge to robust vascular segmentation.

heterogeneous intensity pattern within the aneurysm, as shown in Figs. 1(a) and (b). These inhomogeneous subregions are a challenge if vascular segmentation is to be robust. This work was motivated by the need to develop a fully automatic segmentation algorithm that could reliably segment the vasculature including aneurysms, vessels at the vicinity of the aneurysms and other regions of low or complex flow from PC-MRA data.

A variety of approaches have been proposed for the segmentation of MRA speed images. For instance, Verdonck et al. (1996) proposed to segment blood vessels by iteratively estimating vessel centre axes and contours based on the maximum gradient points. McInerney and Terzopoulos (1997) proposed topologically adaptable surfaces (T-surfaces), which is a variant of the classical deformable models but has an efficient topologically adaptable property for segmentation of intracranial vasculature. Another variant, geodesic active contour was proposed to segment MRA speed images by Lorigo et al. (1999). In this case, the contour was implemented by using the level set methods (Sethian, 1999) to offer flexible topological adaptability, and has been subsequently extended to be more locally adaptable according to the properties of local geometrical structure, for example, eigenvalues of the tensor (Westin et al., 2000). A fast vessel delineation method was suggested by iteratively reconstructing a vessel segment defined by two user specified starting and end points (Wink et al., 2000). In all of these methods, an intensity-based gradient function was employed to estimate the boundaries of vessels. A drawback in using a gradient-based method is that, in practice, gradient values are not sufficiently high in the low or complex flow regions for robust segmentation. Krissian et al. (1998, 1999) proposed a multiscale method to detect the vessel centreline and estimate vessel width based on eigenvalue and eigenvector analysis of the Hessian matrix. However, as with the intensity-based gradient methods, partial differentiation of the MRA speed images will not give reliable information about the position of a vessel boundary in low flow or signal-to-noise ratio (SNR) regions.

An alternative approach to reconstructing vascular shape, proposed by Masutani et al. (1998), consists of initial shape extraction followed by region-growing. The initial shape is obtained by thresholding. Then, a seed point is placed manually inside the initial bounded space and is grown to extract a locally smooth surface by using binary mathematical morphological operations. The major advantages of this method are that thin contacts by the adjacent vessel clusters can be removed and the disconnected clusters of vessels can be grouped. However, due to the low SNR values inside an aneurysm, the aneurysmal and low SNR regions will not always be extracted as the clusters in the initial bounded space. Finally, based on the knowledge of MRA image acquisition, it has also been shown that the accuracy of vessel width estimation can be improved by incorporating a boundary criterion, which is defined as a percentage roll-off factor with respect to maximum luminal MR signal (Frangi et al., 1999).

Wilson and Noble (1999) used an adaptive statistical segmentation method for TOF-MRA data. In the current paper, we extend that statistical method to PC-MRA data. There are two main reasons for this. Firstly, the statistical characteristics of the background and vascular signals can be accurately modelled based on the knowledge of image formation. Secondly, most of the previous segmentation

methods segment the vasculature by using PC-MRA speed images alone. Rather than using just speed information, the directional flow field (available in PC-MRA data only) may give additional clues for segmentation. To the best of our knowledge, there is only one related work (Summers et al., 1997) using both MRA speed and phase images, which uses a multi-resolution, model-based approach to extract and visualize vascular flow features.

The method we propose draws on the fact that the flow pattern in the vasculature is locally coherent. In other words, if blood is flowing in a direction v, neighbouring voxels should have a high probability of exhibiting flow in the same direction v. A local phase coherence (LPC) measure can be derived to estimate the degree of coherence amongst neighbouring voxels. In this paper, we present a statistical approach, which incorporates the LPC measure as a priori knowledge in a Markov random field (MRF) model to improve the quality of vascular segmentation. Related work can be found in the literature of MRF-based segmentation of conventional MR images, rather than MRA, including mean field approximation (Kapur et al., 1998), simulated annealing (SA) and iterated conditional modes (ICM) (Held et al., 1997) and hidden Markov random fields (Zhang et al., 1999). In this paper, we employ ICM to perform a maximum-a-posteriori (MAP) estimation purely because of its efficiency. A thorough comparison of different maximisation methods can be found in (Li, 1995).

Moreover, in this paper, we derive the background and vascular signal statistical models based on knowledge of the MRA image formation process and physical characteristics of blood flow, and use them to derive update equations for expectation-maximisation (EM) based parameter estimation. In particular, we show that the proposed Maxwell–Gaussian finite mixture distribution represents the background signal more accurately than a Maxwell distribution used in prior work (Andersen and Kirsch, 1996). The proposed model shows a better fit to clinical data and gives fewer false positive voxels (misclassified vessel voxels) in segmentation.

This paper is organised as follows. In Section 2, we derive the statistical distributions of background and vascular signals in MRA speed images. Section 3 presents an initial EM based segmentation algorithm based on these models and illustrates the problem of segmentation by using the MRA speed images alone. We then define a local phase coherence measure using three orthogonal phase images and further modify the segmentation algorithm by incorporating the MRF a priori model based on the LPC measure. In Section 4, we present in-vitro and in-vivo experimental segmentation results on an aneurysm phantom and clinical data sets. We conclude with a summary and a discussion of current and future work in Section 5. Early versions of this work were presented at the third conference on Medical Image Computing and Computer-Assisted Intervention (Chung and Noble, 2000).

2. Statistical analysis of background and vascular signals

This section derives statistical distributions for the target vascular signals in MRA speed images as well as for background regions containing static, signal generating tissues (brain, CSF and scalp) or signal-absent material (air, cortical bone) in accordance with the PC-MRA image reconstruction process and physical characteristics of blood flow. These two models are then combined additively to form a complete distribution of an MRA speed image.

2.1. Construction of speed images

2.1.1. Definition of MR phase angle and its properties

The phase angle of a complex-valued MR signal S_1 is defined as ϕ_1 and computed by $\arg(S_1) = \tan^{-1}(\mathrm{Im}\{S_1\}, \mathrm{Re}\{S_1\})$, where $\mathrm{Re}\{S_1\}$ and $\mathrm{Im}\{S_1\}$ denote real and imaginary components of the signal respectively, as illustrated in Fig. 2. It is assumed that the real and imaginary components are statistically independent and corrupted by zero-mean Gaussian noise with equal variance σ^2 (Henkelman, 1985). The probability density function (PDF) of ϕ_1 is then given by (Lathi, 1983),

$$f_{\phi_1}(\phi_1) = \frac{\exp(-\alpha^2)}{2\pi} \times\{1 + \sqrt{\pi}\alpha\cos(\phi_1 - \overline{\phi_1})\exp(\alpha^2\cos^2(\phi_1 - \overline{\phi_1})) \times[1 + \mathrm{erf}(\alpha\cos(\phi_1 - \overline{\phi_1}))]\}, \quad (1)$$

where $\phi_1 \in [-\pi, \pi)$, $\alpha = M_1/\sqrt{2}\sigma$, $\mathrm{erf}(x) = (2/\sqrt{\pi})\cdot\int_0^x e^{-w^2}dw$ is the error function, $\overline{\phi_1}$ is the mean phase and M_1 is the magnitude of signal S_1. Note that $f_{\phi_1} = 0$ for $\phi_1 \notin [-\pi, \pi)$. The PDFs at different signal-to-noise ratios ($SNR = M_1/\sigma = 0$, 1, 3 and 6) are plotted in Fig. 3. Note

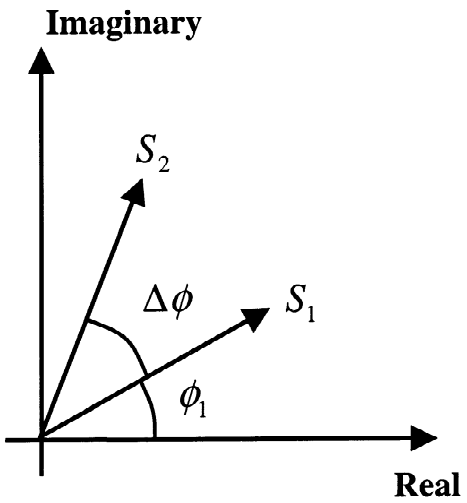

Fig. 2. Difference between phase angles of two signals gives the velocity induced phase shift $\Delta\phi = \phi_2 - \phi_1$.

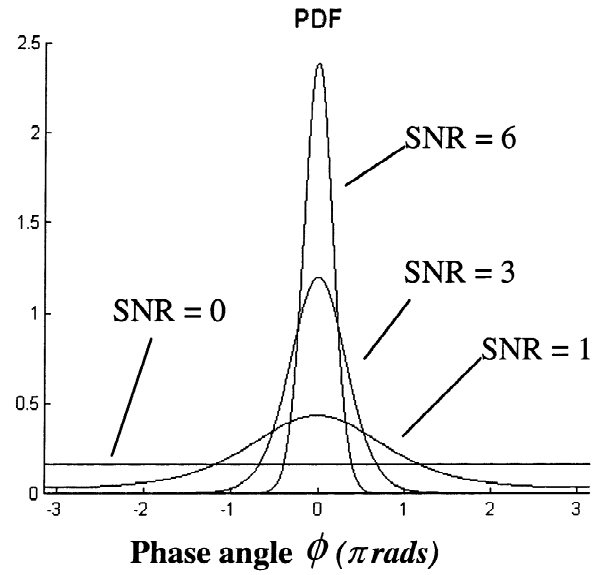

Fig. 3. Probability density functions (PDF) of a phase angle ϕ_1 for different signal-to-noise ratios (SNR). Note that the PDF becomes uniformly distributed when the SNR is zero, and tends to a Gaussian distribution when the SNR is sufficiently high.

that the PDFs progress from being uniformly distributed when the SNR is zero, to Gaussian distributed when the SNR is high.

2.1.2. Definition of speed image and its properties

For each velocity component at a voxel, two complex-valued signals, S_2 and S_1, are acquired. These signals experience the same pulse sequence excitation and spatial encoding during imaging but differ by the polarity or strength of a bipolar gradient applied along the axis of the velocity component being measured. A velocity induced phase shift (phase difference) $\Delta\phi$ is produced by the angular difference between the two signal phases (Pelc et al., 1991), i.e. $\Delta\phi = \phi_2 - \phi_1 = \arg(S_2) - \arg(S_1)$, as shown in Fig. 2. The resulting net phase $\Delta\phi$ for a voxel is directly proportional to the flow rate of material in the voxel in the specified direction. An MRA speed image is reconstructed on a voxel-by-voxel basis by taking the modulus of the three corresponding phase shifts, $\Delta\phi_x$, $\Delta\phi_y$ and $\Delta\phi_z$, and applying an average magnitude mask $\overline{M}$ to suppress the spurious phase shifts in extremely low signal regions (e.g. background air), i.e.,

$$i = \overline{M}\sqrt{\Delta\phi_x^2 + \Delta\phi_y^2 + \Delta\phi_z^2} = \sqrt{(\overline{M}\,\Delta\phi_x)^2 + (\overline{M}\,\Delta\phi_y)^2 + (\overline{M}\,\Delta\phi_z)^2}, \quad (2)$$

where i is the image intensity and $\overline{M} = \Sigma_{n=1}^{N_{acq}} S_n / N_{acq}$ is the average magnitude of all signals acquired at the same voxel. The number of acquisitions (N_{acq}) at each voxel depends on the pattern of bipolar gradients applied: for a six-point reconstruction method ($N_{acq} = 6$) a pair of oppositely oriented bipolar gradients are used for each velocity component, while for a four-point reconstruction method ($N_{acq} = 4$) a single image acquired with a null bipolar gradient (i.e. no velocity sensitivity) is used in combination with each of three velocity encoded images (Bernstein et al., 1994). We will refer to this reconstructed image as the 'magnitude-weighted speed image' though convention is simply to use the term 'speed image' (since the phase shifts are flow sensitized along the three orthogonal components, x, y and z, the result is directly proportional to the speed).

2.2. Statistical analysis of vascular signals

In modelling the intensity characteristics of vessel voxels, we assume a laminar flow pattern is present. In this case, for a circular vessel cross-section, the velocity flow is then parabolic (Caro et al., 1978), as shown in Fig. 4, and the intensity profile for a vessel is given by

$$i(r) = C \cdot \left(1 - \frac{r^2}{R^2}\right), \quad (3)$$

where i is the intensity and is a function of r, C is a constant (incorporating the signal magnitude M), R is the vessel radius and r is the distance from the vessel centre to the boundary. The PDF $f_{vessel}(i)$ for a vessel voxel that has intensity i is directly proportional to the image area, $a(x = i)$, in which all the voxels have the same intensity i. $f_{vessel}(i)$ is calculated as the rate-of-change of area having intensity greater than or equal to i, i.e.,

$$f_{vessel}(i) \propto \left| \frac{da(x \geq i)}{di} \right|. \quad (4)$$

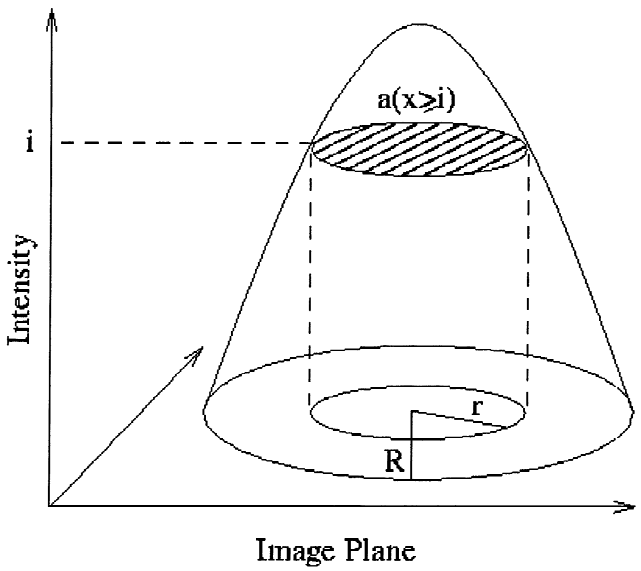

Fig. 4. We assume a vessel model, in which the intensity characteristics of the vessel voxels are assumed to exhibit a laminar flow pattern. The velocity profile across the circular vessel cross-section is then parabolic.

The area $a(x \geqslant i)$ is given by, using Eq. (3),

$$a(x \geqslant i) = \pi r^2 = \pi R^2\left(1 - \frac{i}{C}\right). \tag{5}$$

Therefore, the PDF $f_{\text{vessel}}(i)$ is constant and can be regarded as a uniform distribution, which can be expressed as

$$f_{\text{vessel}}(i) = w_{\text{U}} f_{\text{U}}(i), \tag{6}$$

where w_{U} is a weight (or prior probability) assigned to the uniform distribution, $f_{\text{U}}(i) = 1/I_{\max}$, and $I_{\max}$ is the maximum intensity in the observed frequency histogram. Although, in practice, the vessel voxel intensities mainly spread over the high intensity region, the number of vessel voxels is only a small proportion (1–4%) of the frequency histogram of the entire PC-MRA image volume. Hence, for the sake of simplicity, we assume that the uniform distribution spreads over the entire intensity range $[0 \ldots I_{\max}]$.

2.3. Statistical analysis of background signals

A more involved description is required for signals in regions of background as a wide range of signal intensity and phase shift behaviour may be encountered. In particular, the magnitude of the MR signal from air, for example, is negligible while blood and static tissue have comparable intensities. The effect of noise on the phase angles is modulated by the signal magnitude, with the consequence that the lower the signal intensity, the more uniform will be the distribution of phase differences. In previous work (Andersen and Kirsch, 1996), $\overline{M}\ \Delta\phi_j$ in Eq. (2) (where $j = x,\ y$ or z) was assumed to follow a zero-mean Gaussian distribution. The distribution described by the modulus of three independent zero-mean Gaussians with equal variance σ_p^2 (where p denotes the phase value) is a Maxwell distribution. Hence, according to Eq. (2), the PDF of the background signal is given by a Maxwell distribution (Andersen and Kirsch, 1996; Parzen, 1960),

$$f_{\text{M}}(i) = \frac{2}{\sqrt{2\pi}} \frac{i^2}{\sigma_{\text{M}}^3} \exp\left(\frac{-i^2}{2\sigma_{\text{M}}^2}\right), \tag{7}$$

where $\sigma_{\text{M}} = \sigma_p$ and $i \geqslant 0$. Figs. 5(a) and (b) show a region-of-interest (ROI) inside an in-vivo magnitude-weighted speed image and its corresponding histogram, respectively. A Maxwell distribution was fitted to the histogram by using the relationship $\sigma_{\text{M}} = I_{\text{peak}}/\sqrt{2}$, where I_{peak} is the intensity value at which the histogram achieves its maximum, i.e. $\mathrm{d}f_{\text{M}}(i)/\mathrm{d}i = 0$ at $i = I_{\text{peak}}$. In Fig. 5(b), it is observed that the Maxwell distribution fits well in the low intensity region, but not in the high intensity region (indicated by an arrow in the figure).

The reason for the failure of the Maxwell distribution in describing the background signal is the deviation of the magnitude-weighted phase values $\overline{M}\ \Delta\phi_{\text{j}}$ in Eq. (2) from a Gaussian distribution. Neither of the tails of the magnitude-weighted phase image histogram is properly fitted by a Gaussian distribution when the SNR in the image background is relatively low (indicated by the arrows in Fig. 6(b)). As plotted in Fig. 3, the low SNR makes the distributions of phase angles, ϕ_1 and ϕ_2, deviate from the Gaussian distribution, which in turn affects the shape of distribution of $\Delta\phi$. Together with the Rician nature of

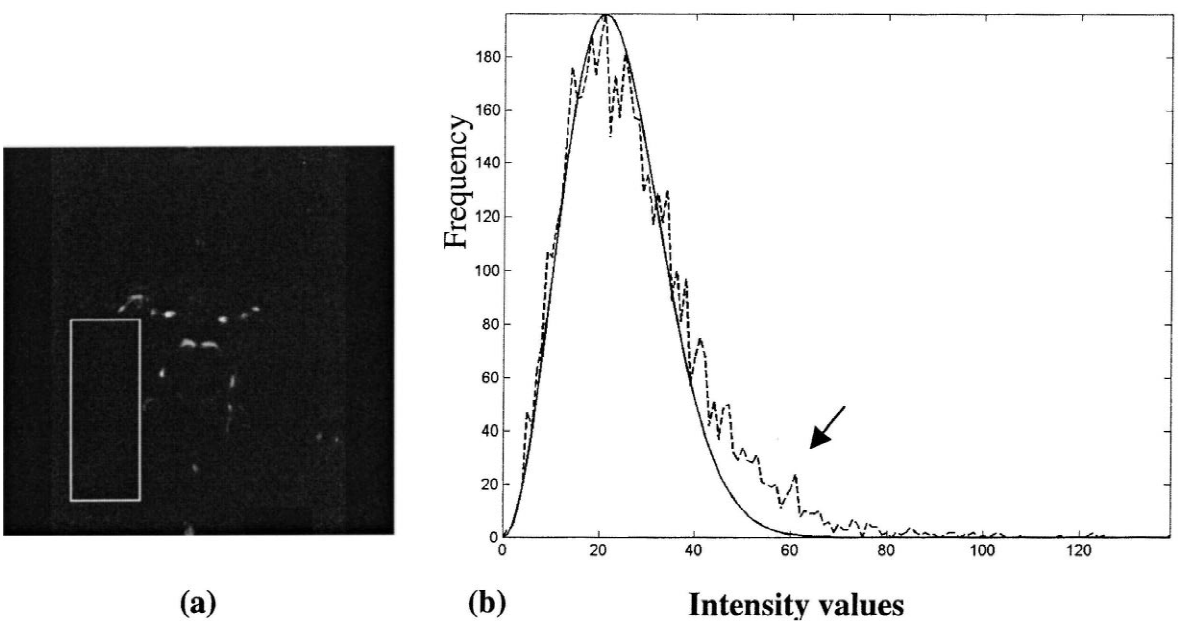

Fig. 5. (a) Region-of-interest (ROI) inside a speed image and (b) its corresponding histogram (dashed), respectively. In (b), observe that the Maxwell distribution (solid) fits well in the low intensity region, but not in the high intensity region (indicated by an arrow in (b)).

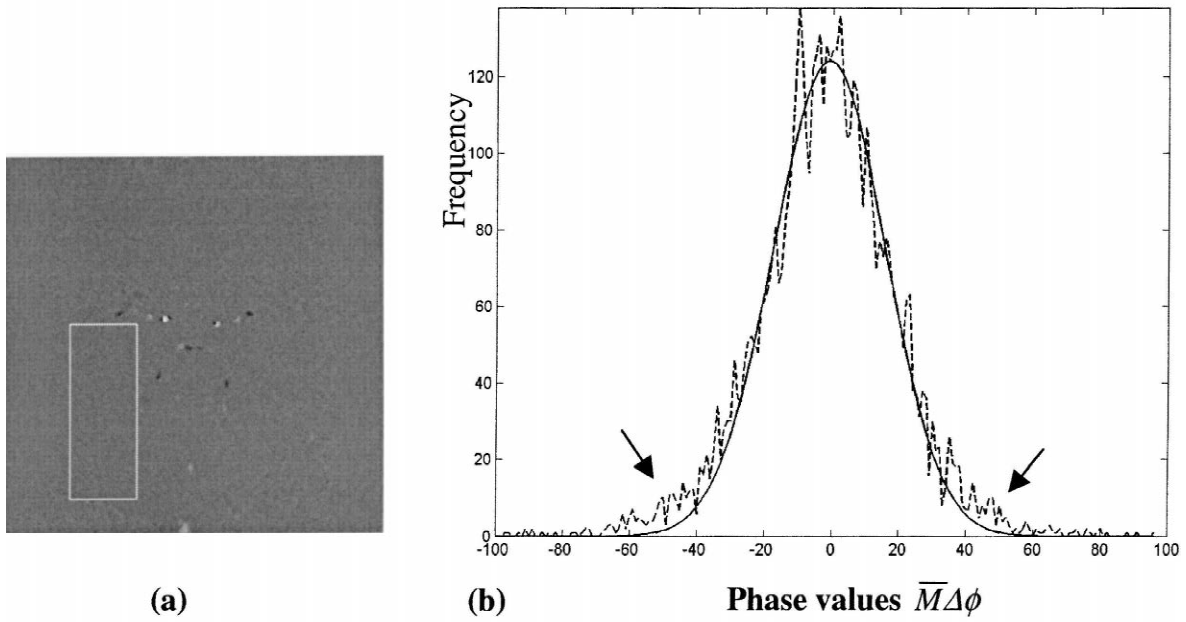

Fig. 6. (a) Region-of-interest (ROI) inside a phase image $\overline{M}\,\Delta\phi$ and (b) its corresponding histogram (dashed). It is observed that both tails of the phase image histogram are not perfectly fitted by a Gaussian distribution (solid) (indicated by the arrows in (b)).

noise in the signal magnitude (Andersen and Kirsch, 1996), it is not surprising that the distribution of their product, the magnitude-weighted phase value $\overline{M}\,\Delta\phi$, is not entirely Gaussian when the SNR is low.

To reduce the error in fitting the background signal, we introduce two small, non-zero mean Gaussian residual distributions to the model of the magnitude-weighted phase values. Thus, for each encoding direction, the PDF of $\overline{M}\,\Delta\phi$ consists of a zero-mean Gaussian (located at the centre) and two non-zero mean Gaussian distributions (located at each side). Fig. 7(a) shows the fitted distribution using one zero-mean Gaussian distribution and two opposite non-zero mean Gaussian distributions. Fig. 7(b) shows the individual distributions. As mentioned earlier, after the modulus operation, a Maxwell distribution is formed by the modulus of the three zero-mean Gaussian distributions, whereas the modulus of the residual non-zero mean Gaussian distributions (with relatively high SNR = 3) gives a Gaussian distribution (Chung, 2001; Andersen and Kirsch, 1996; Gudbjartsson and Patz, 1995). Hence, the PDF of background signal consists of a linear mixture of a Maxwell distribution $f_{\mathrm{M}}(i)$ with variance σ_{M}^2 and a Gaussian distribution $f_{\mathrm{G}}(i)$ with mean μ_{G} and variance σ_{G}^2, i.e.,

$$f_{\mathrm{background}}(i) = w_{\mathrm{M}} f_{\mathrm{M}}(i) + w_{\mathrm{G}} f_{\mathrm{G}}(i), \tag{8}$$

where w_{M} and w_{G} are weights (or prior probabilities)

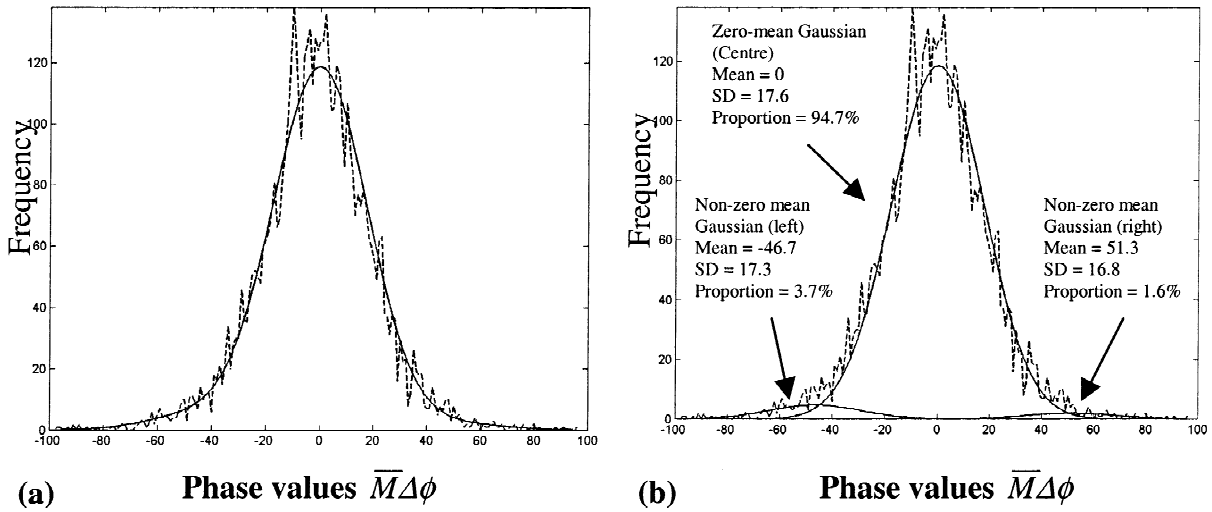

Fig. 7. (a) The fitted distribution (solid) using one zero-mean Gaussian distribution and two opposite non-zero mean Gaussian distributions. (b) It reveals the individual distributions (solid). Dashed histogram shows the given phase image histogram.

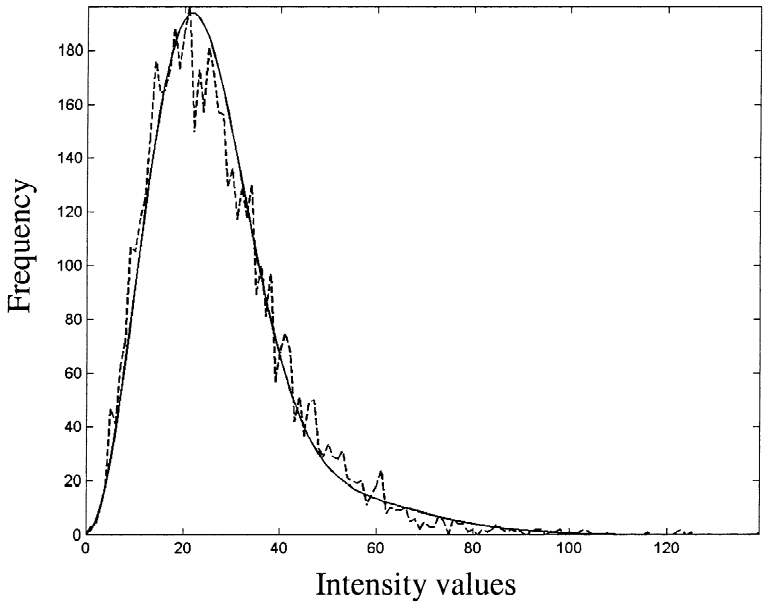

Fig. 8. Histogram of an MRA speed image (solid). The histogram was subsequently fitted by a Maxwell–Gaussian mixture distribution (dashed). It shows that the Maxwell–Gaussian mixture model achieves a better fit than the Maxwell model, as shown in Fig. 5(b).

assigned to the Maxwell and Gaussian distributions, respectively. As shown in Fig. 8, a Maxwell and Gaussian mixture model achieves a better fit to the given histogram of a PC-MRA speed image, as compared with Fig. 5(b) (the fitting procedure used in this case is discussed in Section 3).

2.4. Statistical model for magnitude-weighted speed images

With reference to Eqs. (6) and (8), we conclude that the overall PDF $f(i)$ of a PC-MRA magnitude-weighted speed image can be modelled as the summation of a Maxwell-Gaussian and uniform finite mixture distribution, namely a Maxwell–Gaussian-uniform (MGU) model,

$$f(i) = \underbrace{w_M f_M(i) + w_G f_G(i)}_{\text{Background signal}} + \underbrace{w_U f_U(i)}_{\text{Vascular signal}}, \quad (9)$$

where $w_M + w_G + w_U = 1$.

3. Segmentation algorithm

This section describes the overall segmentation scheme, which has two stages. First, MRA speed images are segmented using the MGU statistical model, (Section 3.1). Second, the result is then treated as an initial estimate of an MRF-based segmentation method (Section 3.2).

3.1. Segmentation based on speed information

3.1.1. Optimisation of statistical model parameters

In Eq. (9), the mixture model has six parameters: w_M, w_G, w_U, σ_M^2, μ_G and σ_G^2, which need to be estimated. The modified EM algorithm can be used to estimate the parameters by maximising the log-likelihood of the mixture distribution at each iteration (Bishop, 1995). As shown in Appendix A, the update equations can be derived. These update equations are listed in Table 1.

In our implementation, the initial estimates of parameters were found automatically. Let $h(i)$, $h_M^{\text{init}}(i)$ and $h_G^{\text{init}}(i)$ be the observed, initial Maxwell and initial Gaussian histograms, respectively. The initial standard deviation of the Maxwell distribution σ_M^{init} is set to $I_{\text{peak}}/\sqrt{2}$. The initial histogram of the Maxwell distribution is then given by $h_M^{\text{init}}(i) = C f_M(i|\sigma_M^{\text{init}})$, where C is set to $(e\sqrt{\pi}/4)h(I_{\text{peak}})I_{\text{peak}}$ to ensure that $h_M^{\text{init}}(I_{\text{peak}})$ has the same height as $h(I_{\text{peak}})$, as

Table 1
Update equations and posterior probabilities at kth iteration for each distribution

Maxwell (M)	$w_M^{k+1} = \frac{1}{N}\Sigma_i h(i)P^k(M\|i)$ and
	$(\sigma_M^2)^{k+1} = \frac{\Sigma_i h(i)P^k(M\|i)i^2}{3\Sigma_i h(i)P^k(M\|i)}$,
	where $P^k(M\|i) = w_M^k f_M^k(i)/f^k(i)$.
Gaussian (G)	$w_G^{k+1} = \frac{1}{N}\Sigma_i h(i)P^k(G\|i)$,
	$\mu_G^{k+1} = \frac{\Sigma_i h(i)P^k(G\|i)i}{\Sigma_i h(i)P^k(G\|i)}$ and
	$(\sigma_G^2)^{k+1} = \frac{\Sigma_i h(i)P^k(G\|i)(i-\mu_G^{k+1})^2}{\Sigma_i h(i)P^k(G\|i)}$,
	where $P^k(G\|i) = w_G^k f_G^k(i)/f^k(i)$.
Uniform (U)	$w_U^{k+1} = \frac{1}{N}\Sigma_i h(i)P^k(U\|i)$,
	where $P^k(U\|i) = w_U^k f_U^k(i)/f^k(i)$ and $f_U^k(i) = 1/I_{\max}$.

illustrated in Fig. 9(a). Let A_M be the area of $h(i)$ covered by $h_M^{init}(i)$, and A_{total} be the total area covered by $h(i)$. Then w_M^{init} is defined as the ratio A_M/A_{total}.

Let $h_{res}(i)$ be the residual histogram, which is computed as

$$h_{res}(i) = \mathrm{abs}\big(h(i) - h_M^{init}(i)\big)u(i - I_{peak}), \tag{10}$$

where $u(i - I_{peak})$ is a step function that ensures that μ_G is larger than I_{peak}. Then, μ_G^{init} and σ_G^{init} are defined as the initial mean and standard derivation of the 95% highest posterior density (HPD) interval of $h_{res}(i)$. The HPD represents most of the mass (95%) of the distribution (Box and Tiao, 1973) and helps to avoid the influence of the long (relatively low value) tail of $h_{res}(i)$ on the estimations of the mean and standard derivation of the initial Gaussian distribution[1]. The initial Gaussian distribution histogram is given by $h_G^{init}(i) = Cf_G\big(i|\mu_G^{init},\ \sigma_G^{init}\big)$, where C is set to $\sqrt{2\pi}h_{res}\big(\mu_G^{init}\big)\sigma_G^{init}$ to ensure that $h_G^{init}\big(\mu_G^{init}\big)$ has the same height as $h_{res}\big(\mu_G^{init}\big)$ (see Fig. 9(b)). Let A_G be the area of $h_{res}(i)$ covered by $h_G^{init}(i)$. Then, w_G^{init} is defined as the ratio A_G/A_{total}. Finally, $w_U^{init} = 1 - w_M^{init} - w_G^{init}$ if $w_M^{init} + w_G^{init} <$

[1] A formal definition of HPD interval can be found in (Box and Tiao, 1973). In general, given a probability content (e.g. 95%), the HPD interval occupies the smallest volume in the parameter space (e.g. $[0 \ldots I_{max}]$), which contains most (95%) of the probability. Moreover, the probability density of every point inside the HPD interval is at least as large as that of any point outside it.

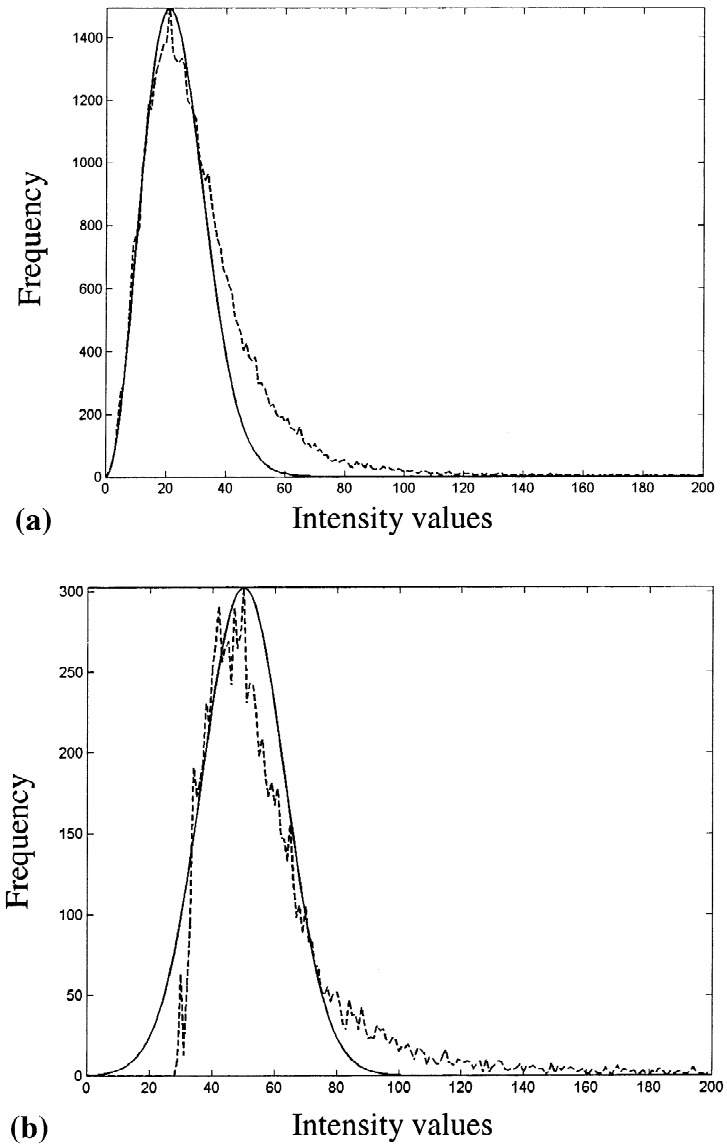

Fig. 9. (a) The observed histogram $h(i)$ (dashed) and the initial histogram of the Maxwell distribution $h_M^{init}(i)$ (solid). (b). The residual histogram $h_{res}(i)$ (dashed) and the initial histogram of the Gaussian distribution $h_G^{init}(i)$ (solid).

1. Otherwise, the values of w_M^{init}, w_G^{init} and w_U^{init} are set to the empirical values, which are needed purely for ensuring the robustness of the method. We have found that the convergence of the modified EM algorithm is generally reached after 10–20 iterations.

An example of the performance of the MGU model applied to a clinical MRA speed image is shown in Fig. 10(a). For comparison, a Maxwell and uniform mixture model has been fitted using the modified EM algorithm in Fig. 10(b). The MGU mixture model shows a noticeable improvement over the Maxwell-uniform model in fitting the background signal. It is worth noting that, in practice, together with the imperfection of the Maxwell background signal model, ghosting artifacts and partial volume effect also contribute to the poorer fit of the Maxwell model in the clinical data.

3.1.2. Determination of magnitude-weighted speed image threshold for segmentation

Given an estimated mixture model, voxels on an MRA speed image can be segmented into two classes, v and b denote vessel and background, based on the maximum-a-posteriori (MAP) criterion. Assume that the weights (or prior probabilities) remain constant. Then, using the MAP criterion, a voxel is set to class v when the vessel probability $w_U f_U(i)$ is greater than the background probability $w_M f_M(i) + w_G f_G(i)$. A threshold can be defined at the intersection of the background and vessel probability

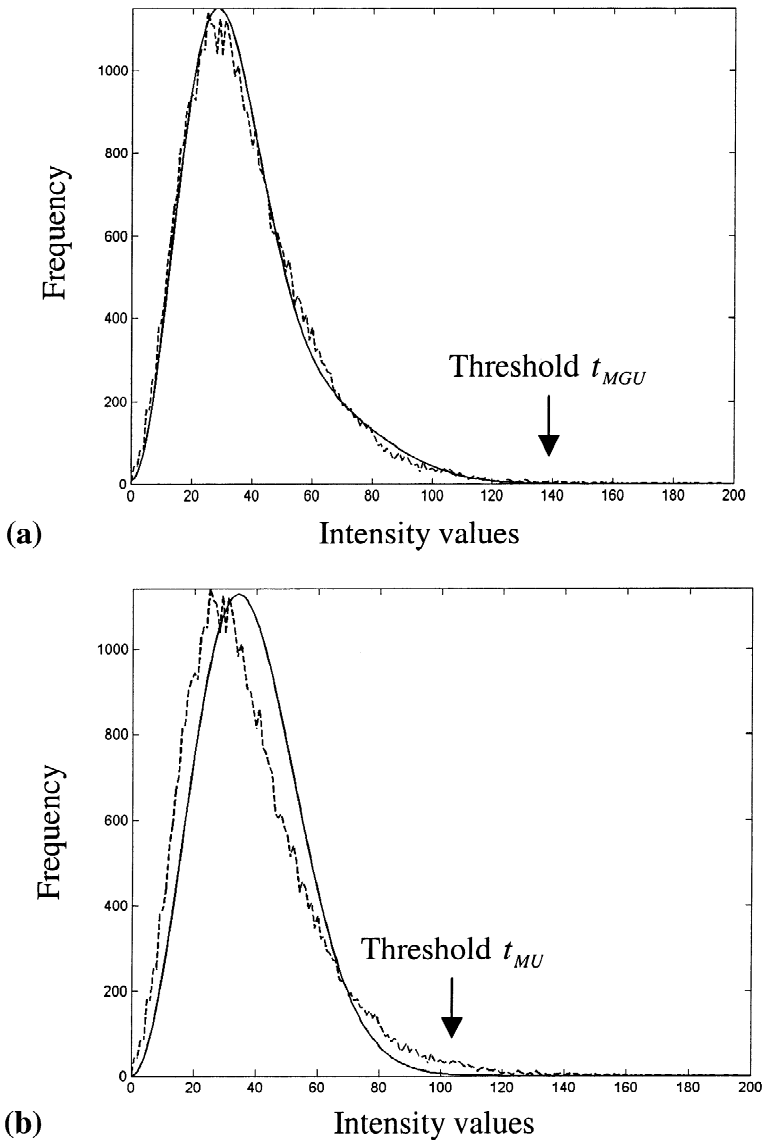

Fig. 10. (a) Histogram of an MRA speed image (dashed) and the Maxwell–Gaussian-uniform (MGU) mixture model (solid). The threshold t_{MGU} found by using MGU model tends to be more correct and is usually higher than the threshold t_{MU} found by using MU model (as compared with (b)). (b) Histogram of an MRA speed image (dashed) and the Maxwell-uniform (MU) mixture model (solid).

distributions. As indicated by the arrows in Figs. 10(a) and (b), the threshold t_{MGU} found based on the MGU model tends to be more correct and is usually higher than the threshold t_{MU} found by using the Maxwell-uniform (MU) model. As shown in Figs. 11(a) and (b), fewer false positives (misclassified vessel voxels) are detected if the threshold t_{MGU} is used in the segmentation process (the original MRA speed image is shown in Fig. 5(a)).

3.1.3. Problem of segmentation based on speed information alone

Figs. 12(a) and (b) show an MRA speed image and a binary-segmented image produced using the MGU model and the MAP classification method. The aneurysm is indicated by an arrow in the figure. Note that the resulting segmentation is adversely affected by the significant signal loss inside an aneurysm located at the middle. This causes some of the intensity values to drop gradually to as low as that of background voxels. The same is seen in Figs. 13(a) and (b). We will discuss how to overcome this problem in the next subsection.

3.2. Integration of phase information into the segmentation

In this section, we define a local phase coherence (LPC) measure, and propose an automated threshold determination method applicable to the thresholding of LPC map. To improve the quality of segmentation, the combination of the LPC measure and speed information in the segmentation process is described.

3.2.1. Definition of local phase coherence

Figs. 14(a) and (b) show the flow pattern in an aneurysm. It can be seen that there is (a) a vortex centred at the singular point, at which the velocity becomes null, and (b) a locally linear (coherent) motion around the neighbourhood of the singular point, which can also be regarded as a deformed circular flow. This is consistent with the results of clinical flow studies (Gobin et al., 1994; Low et al., 1993; Strother et al., 1992) and simulations of computational fluid dynamics (Foutrakis et al., 1999; Ortega, 1998; Burleson et al., 1995). The locally linear motion exists not only inside the aneurysm, but also in most of the vasculature having a laminar flow pattern.

Let us consider a way to quantify locally linear motion. Let $V=\{v_1, \ldots, v_N\}$ be a velocity map, where N is the total number of voxels. Also let the three orthogonal velocity components of a voxel be assigned as the phase shifts along the corresponding scanning direction, i.e. for $v_s=(v_s^x, v_s^y, v_s^z)$, $v_s^x=\Delta\phi_x$, $v_s^y=\Delta\phi_y$ and $v_s^z=\Delta\phi_z$. We define a phase feature P as the cosine of the angle between the velocity v_s at voxel s and the velocity v_t of its neighbouring voxel t, where $s\in[1\ldots N]$. The phase feature P is given by a dot product of the two normalised velocities, $P(v_s, v_t)=v_s v_t/(\|v_s\|\cdot\|v_t\|)$, where $P\in[-1, 1]$. To quantify the locally linear motion around voxel s, we measure its LPC by applying an in-plane 3×3 voxel mask centred at s to the velocity map. LPC is defined by considering the locally coherent motion of its 8 neighbouring voxels,

$$\mathrm{LPC}(s)=P(v_1, v_2)+P(v_2, v_3)+\cdots+P(v_8, v_1), \qquad (11)$$

where $\mathrm{LPC}(s)\in[-8, 8]$ and v_i are numbered as in Fig. 15. In other words, LPC is a circular addition of dot products of the 8 adjacent normalised velocity pairs, and captures the local flow-based textural information about

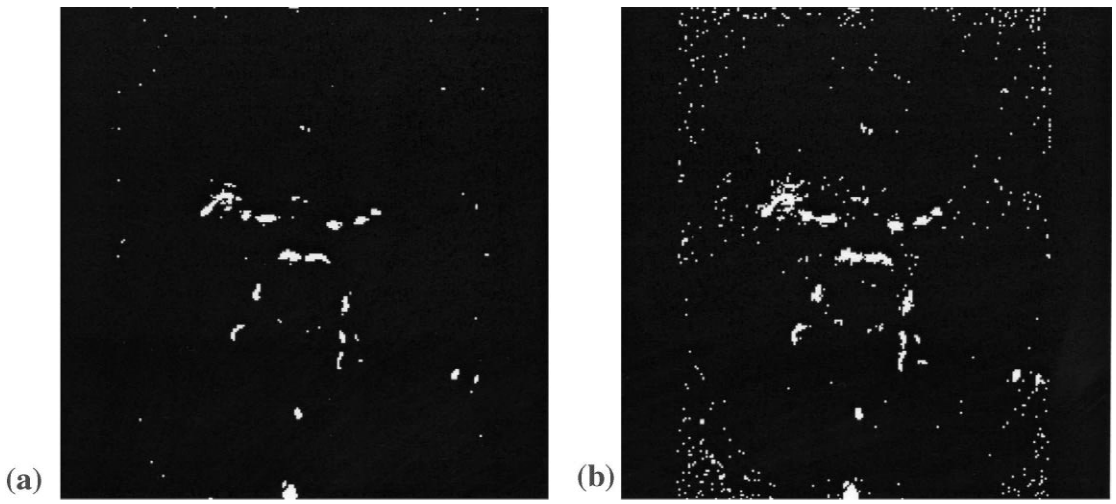

Fig. 11. (a) A segmented image using a threshold t_{MGU} found by employing the MGU model. (b) A segmented image using a threshold t_{MU} found by employing the MU model. These figures show that fewer false positive voxels (misclassified vessel voxels) will be detected if the threshold t_{MU} is used in the segmentation process (the original MRA speed image is shown in Fig. 5(a)).

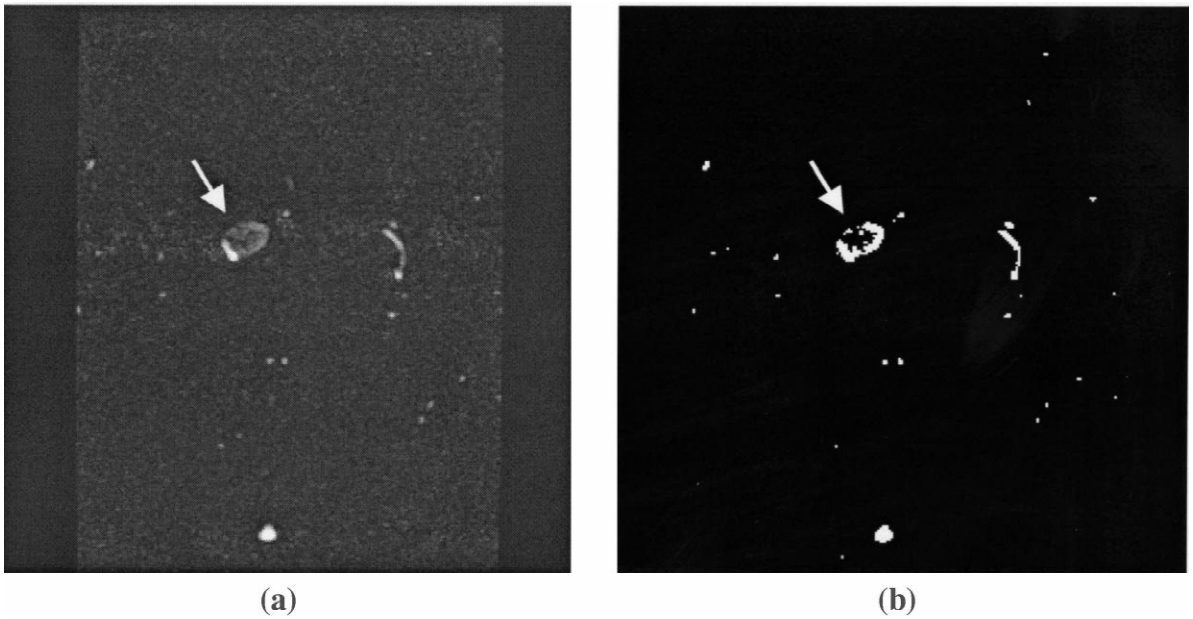

Fig. 12. Patient 1. (a) An MRA speed image and (b) a binary-segmented image produced using the Maxwell–Gaussian-uniform (MGU) model and a MAP classification method. The aneurysm is indicated by an arrow in the figure. It is noted that the resulting segmentation is adversely affected by the significant signal loss inside an aneurysm located at the middle. The same happens in Figs. 13(a) and (b).

the coherence of motions within a pre-defined (3×3) voxel mask. Fig. 16 shows an LPC map for the MRA speed image of Fig. 12(a), in which the image intensity value is directly proportional to the strength of LPC. Observe that the voxels inside the aneurysm and vessels exhibit high LPC and form a piece-wise homogeneous region, whereas the non-vessel voxels have relatively low and random valued LPC.

3.2.2. Automated threshold determination for the LPC map

We now present an automatic threshold determination

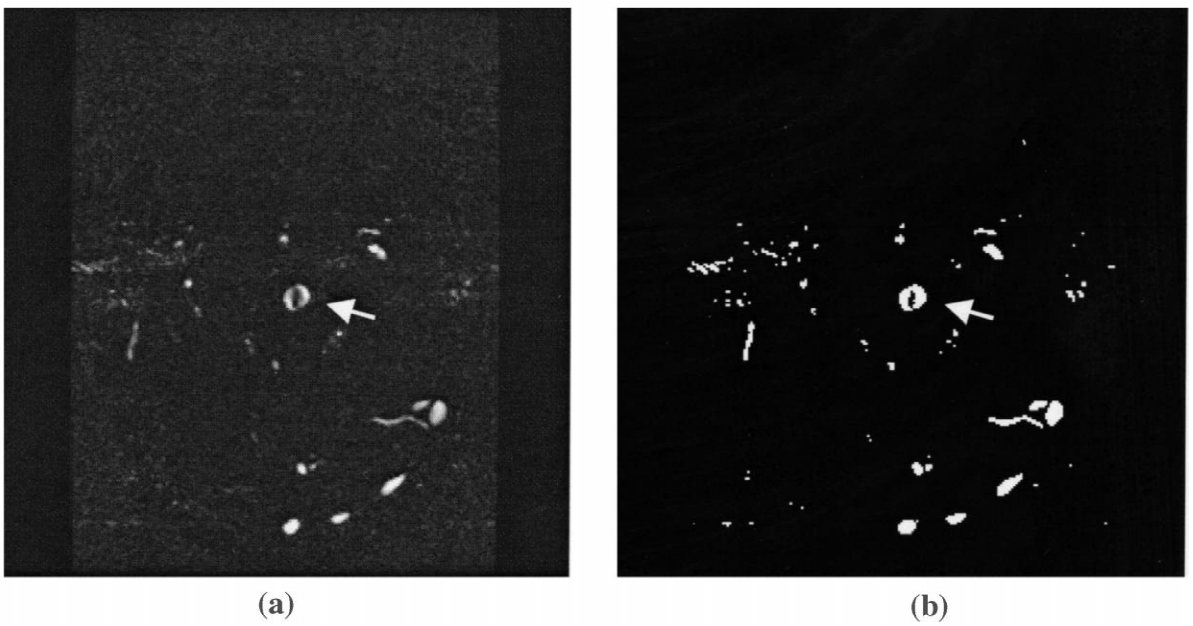

Fig. 13. Patient 2. (a) An MRA speed image and (b) a binary-segmented image produced using the Maxwell–Gaussian-uniform (MGU) model and a MAP classification method. The aneurysm is indicated by an arrow in the figure. It is noted that the resulting segmentation is adversely affected by the significant signal loss inside an aneurysm located at the middle. The same happens in Figs. 12(a) and (b).

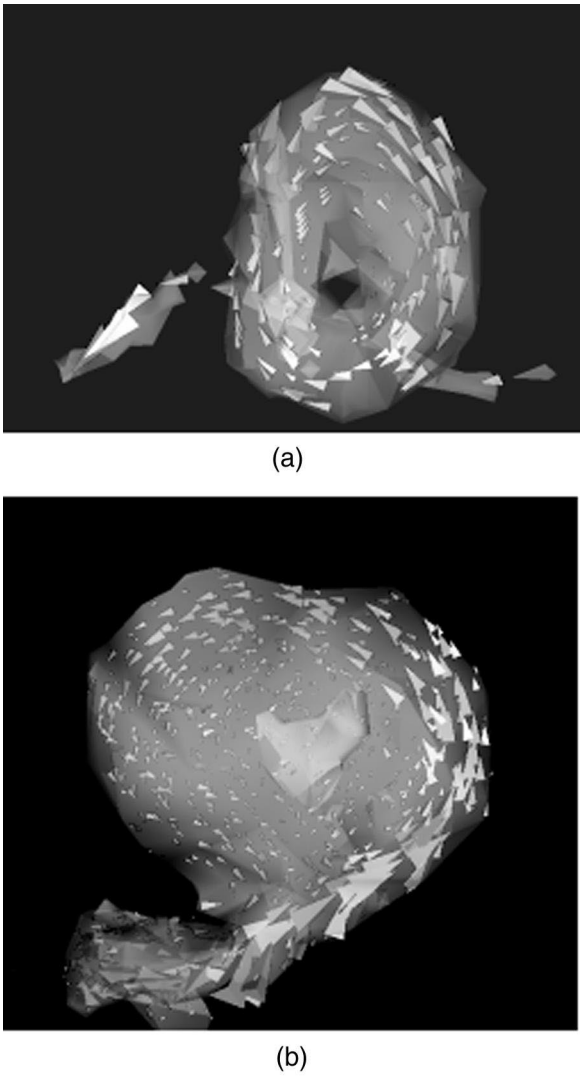

Fig. 14. The flow patterns in the aneurysms. Each flow vector is represented by a cone. The vertex of each cone indicates the flow direction. The flow patterns appear to show (a) a vortex centred at the singular point, at which the velocity becomes null, and (b) a locally linear (coherent) motion around the neighbourhood of the singular point, which can also be regarded as a deformed circular flow.

method for classification of coherent and non-coherent voxels in an LPC map. A histogram of an LPC map is plotted in Fig. 17. It shows that the histogram is right shifted and skewed. In fact, the LPC histogram can be

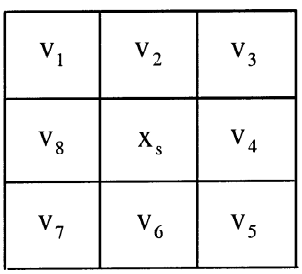

Fig. 15. The 8 neighbouring velocities of voxel x_s.

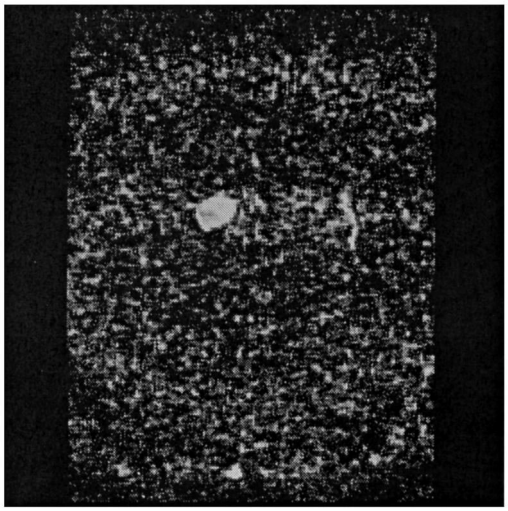

Fig. 16. Local phase coherence map.

described by three classes: *background* with low LPC, *brain tissue* with slightly higher LPC, and *vessel* with high LPC, which are shown in Figs. 18 and 19. Background (B) and brain tissue (T) histograms overlap heavily because of the non-stationary, but slightly coherent, motion of the non-vessel brain tissue. By contrast, the vessel (V) histogram is separated clearly from the background (B) histogram. The point of separation—the desired threshold—is indicated by an arrow in Fig. 19. We model the background region and non-background regions, including vessel and brain tissue, with two separate Gaussian distributions. It is worth noting that theoretical modelling of the LPC histogram is extremely difficult because of the high correlation between the velocity random variables, and normalisation and dot product operations of the correlated variables in Eq. (11). A Gaussian distribution is employed to model the non-background regions including both T and V histograms. This is because the V histogram overlaps heavily with the T histogram, and occupies only a small portion (1–4%) of the LPC histogram. Moreover, as will be

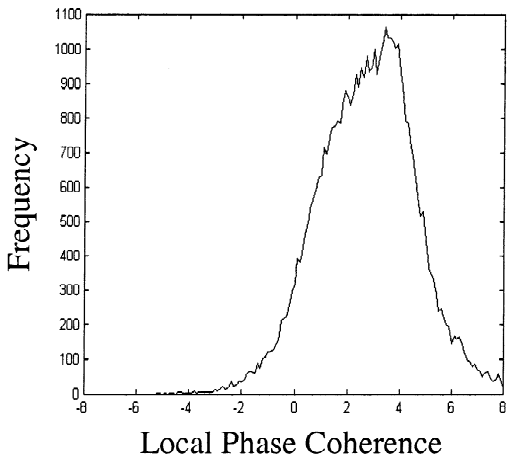

Fig. 17. Histogram of the local phase coherence map of Fig. 16.

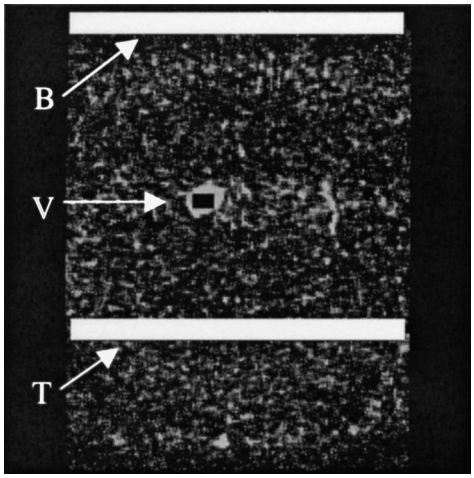

Fig. 18. Regions of interest (black and white boxes). B: background; V: vessel and T: brain tissue.

discussed below, estimation for the B histogram is far more important than that for the T and V histograms.

Again, we use the modified EM algorithm (Bishop, 1995) to fit the LPC histogram by a mixture of the two Gaussian distributions, as shown in Fig. 20. Note that the two estimated Gaussians merge together and form a smooth curve because the means of the two Gaussians are close to each other (in this case, 1.6 for background and 3.7 for non-background) and variances are relatively large and roughly the same (in this case, 2.9 for background and 2.2 for non-background). We define the mean and variance of the background distribution as μ_B and σ_B^2, respectively, and use $\mu_B + \alpha\sigma_B$ as a background threshold ($\alpha = 2$ or 3 depending on the actual variation of background LPC values in the MRA data. We set α equal to 3 in this paper), which is a variant of the background thresholding approach (Brummer et al., 1993; Atkins and Mackiewich, 1998). A voxel with LPC above the background threshold is labelled

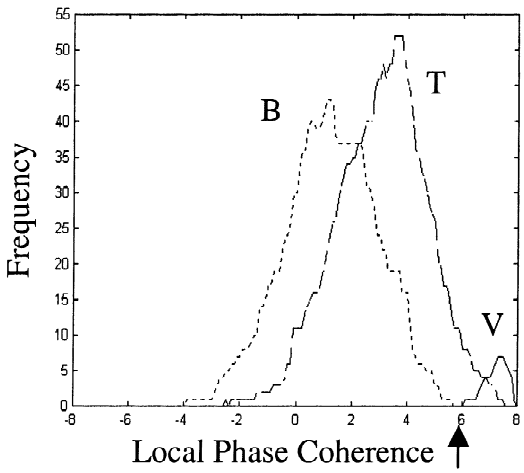

Fig. 19. Individual histograms of regions of interest in Fig. 18. Arrow denotes threshold between tissue (dashed) and vessels (solid). Clear separation is seen between the vessel and background (dotted).

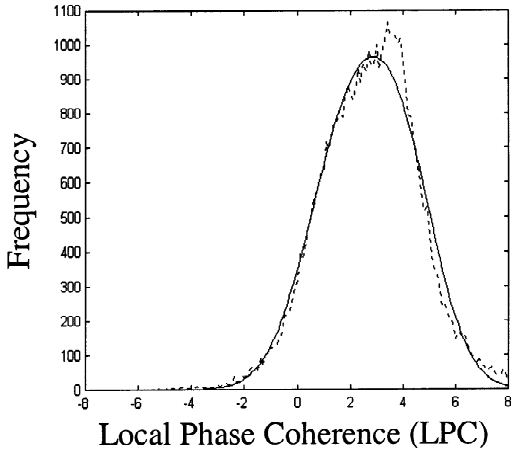

Fig. 20. Histogram of LPC map (dashed) and fitting of the two-Gaussian model (solid).

as a *coherent* voxel. Otherwise, it is labelled as a *non-coherent* voxel. As shown in Fig. 21, the coherent voxels form a number of vessel 'clusters', though there are some randomly distributed voxels due to random coherent noise, small coherent motion of the non-vessel tissue during scanning and ghosting artifacts. These 'outliers' can be ignored if they are far away and disconnected from the vasculature, and their intensity values in a speed image are low.

3.2.3. Combining magnitude-weighted speed and LPC image analysis for segmentation

To improve the quality of the speed-based segmentation described in Section 3.1, we extend the segmentation process through the use of information about the flow coherence of flowing blood (LPC measure) in the segmentation process.

Let $X = \{x_1, \ldots, x_N\}$ be the true-segmented image, where $x_s \in \{v, b\}$ and N represents the total number of voxels in an image and let $I = \{i_1, \ldots, i_N\}$ be the observed MRA speed image, where $i_s \in [0 \ldots I_{max}]$. Then, our goal is to

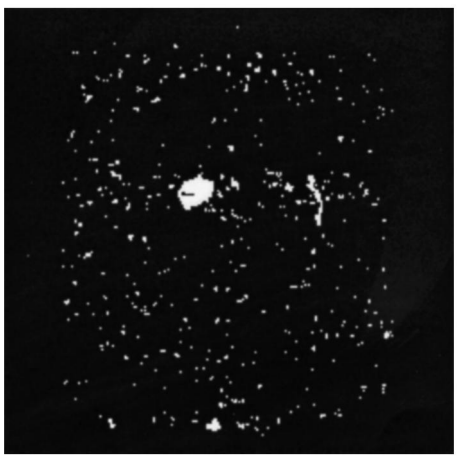

Fig. 21. Coherent voxels.

maximise the probability of estimating the true-segmented binary image given the observed image, i.e. $P(X|I)$. By Bayes' theorem $P(X|I) \propto P(X)P(I|X)$, where $P(I|X)$ represents the likelihood function of the observed image given the knowledge of the image formation, and $P(X)$ represents the prior probability of the true image.

It is assumed that the observed intensity i_s at each voxel S is conditionally independent of the other voxels. The likelihood function is then given by

$$P(I|X) = \prod_{s=1}^{N} P(i_s|x_s), \tag{12}$$

where, using the parameters estimated by the modified EM algorithm in the previous section, the vessel likelihood $P(i_s|x_s = v)$ and background likelihood $P(i_s|x_s = b)$ at each voxel are defined as

$$f_U(i_s) \quad \text{and} \quad \frac{[w_M f_M(i_s) + w_G f_G(i_s)]}{(w_M + w_G)}, \tag{13}$$

respectively. As described in Section 3.1, with the prior probability $P(X)$ assumed constant, each voxel in an MRA speed image is initially classified as one of the states, $\{v, b\}$, by using the MAP method. This is used as a starting point of the *Markov random field* (MRF) based segmentation.

The LPC measure and the current state of each voxel are treated as a priori knowledge to define the prior probabilities of the vessel and background at each voxel. A MRF framework is used because the local relationship between neighbouring voxels can be enhanced in the segmentation process. Rather than using a global, constant threshold (as in Section 3.1), the local threshold at each voxel is made adaptive (Pappas, 1992) and depends on the LPC measure and current tissue type of the surrounding voxels. According to the Hammersley–Clifford theorem (Geman and Geman, 1984), the prior probability is given by a Gibbs function. With the assumptions that the state of each voxel is dependent only on the immediate in-plane 8 neighbours, a second-order neighbouring system can be defined with 8 two-site cliques, $c = \{1, \ldots, 8\}$, for each voxel at the centre of a 3×3 window, as illustrated in Fig. 22. The prior probability $P(x_s)$ and the total energy function $U(x_s)$ for voxel s are defined as

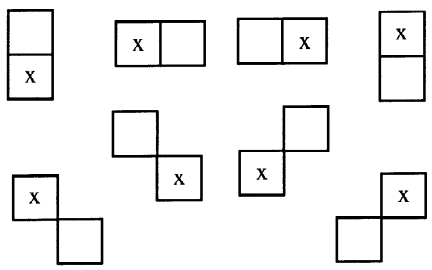

Fig. 22. The 8 two-site cliques. The centre of the 3×3 mask is labelled as x.

$$P(x_s) = Z^{-1} \exp\{U(x_s)\} \quad \text{and} \quad U(x_s) = \sum_{c=1}^{8} E_c(x_s), \tag{14}$$

where $Z = \Sigma_{x_s \in \{v,b\}} \exp\{U(x_s)\}$ is a normalisation constant. These interactions among the voxels are measured by a clique energy function $E_c(x_s)$, which encourages LPC homogeneity and discourages the 'outlier' voxels far away from the vasculature. As such, the clique energy functions for the vessel and background voxels are defined as

$$E_c(x_s = v) = \begin{cases} \beta_v, & \text{if } x_c = v, \text{ and } x_s \text{ and } x_c \text{ are coherent,} \\ 0, & \text{otherwise,} \end{cases}$$
$$E_c(x_s = b) = \begin{cases} 0, & \text{if } x_c = v, \text{ and } x_s \text{ and } x_c \text{ are coherent,} \\ \beta_b, & \text{otherwise.} \end{cases} \tag{15}$$

In practice, we set both β_v and β_b equal to 1. As such, the Markov prior probability of vessel $P(x_s = v)$ is directly proportional to the multiplier of the number of adjacent, and coherent, vessel voxels, whereas the background prior probability $P(x_s = b)$ is directly proportional to the multiplier of the number of non-coherent or non-vessel voxels.

Note that in similarity to the standard anisotropic Potts model, which weights cliques according to their orientations, β_v and β_b could be set to different values. For instance setting β_v to a higher value (e.g. 2 or higher) would enhance the interactions between the coherent, vessel voxels (Ripley, 1991; Li, 1995; Mignotte et al., 1999).

The iterated conditional modes (ICM) (Besag, 1986) algorithm is employed to maximise the probability of the true-segmented binary image given the observed image, i.e. $P(X|I)$, by changing the tissue type (vessel or background) at each voxel according to the LPC measure and current tissue type of neighbouring voxels. The true segmentation X is initialized using the segmentation results based on speed information, as shown in Figs. 12(b) and 13(b). The ICM algorithm estimates a voxel class by using the MAP method, $x_s = \text{argmax}_{x_s \in [v,b]} P(x_s|i_s)$, at each voxel iteratively according to the Bayes' theorem $P(x_s|i_s) \propto P(x_s)P(i_s|x_s)$, where $P(x_s)$ and $P(i_s|x_s)$ are defined in Eqs. (14) and (13), respectively. The iteration process is repeated until the posterior probability is maximised and there is no change in tissue type. Convergence is normally achieved in around 10 iterations.

4. Results

In this section, we present a comparison between the MU model and MGU model in two clinical speed image data sets. Results are also presented on data of one aneurysm phantom and two clinical data sets. We show the improvement of the new approach to segmenting vasculature as well as aneurysms.

4.1. Comparing the MGU and MU models

The purpose of this comparison was to show the difference between the MU and the proposed MGU models for describing statistical characteristics of signals in MRA speed images. Intracranial scans (PC-MRA) of two patients were performed using a 1.5 T GE MR scanner at the Department of Clinical Neurosciences, King's College London. The data volume was $256\times256\times28$ voxels with a voxel size of $0.8\times0.8\times1$ mm^3. The MU model was compared with the MGU model by computing the absolute difference error between the observed histogram and the estimated histogram for all slices (28 slices) in the two scans. Results are plotted in Figs. 23(a) and (b). This shows that Maxwell–Gaussian mixture model is better than the Maxwell model for describing the signal distribution in PC-MRA speed images by an average of 13%.

4.2. Clinical data sets

The new segmentation algorithm was then applied to all slices in the two clinical data sets. The segmentation results are shown in Figs. 24 and 25. Comparing this with the results of Figs. 12(b) and 13(b), it is noted that there is a substantial improvement in segmentation, especially in the region of the aneurysm. However, there are some false negative voxels near the singular point (near the middle of the aneurysm). This is because the level of intensity is very

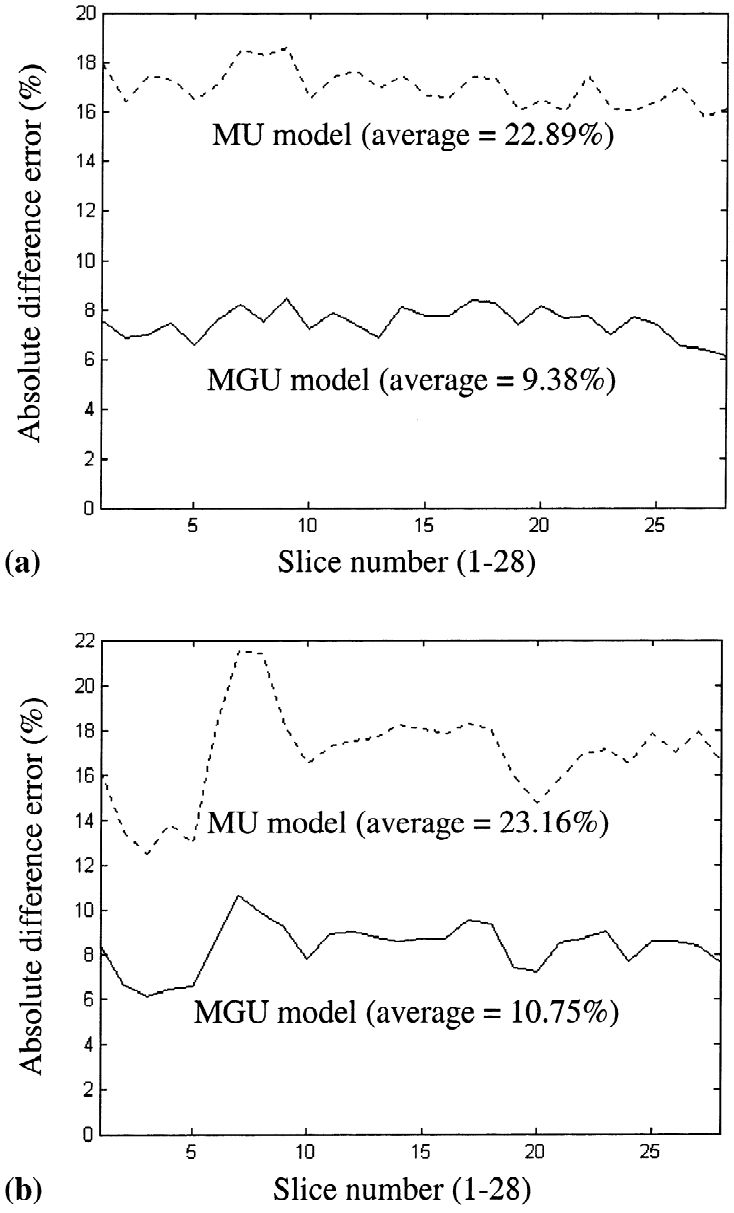

Fig. 23. The MU model (dashed) was compared with the MGU model (solid) by computing the absolute difference error for all slices in the two scans. This shows that the MGU model is better than the MU model for describing the signal distribution in PC-MRA speed images by an average of 13%.

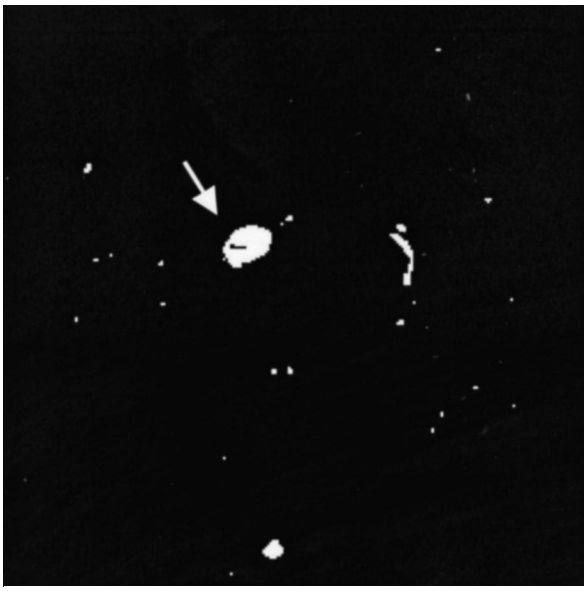

Fig. 24. Patient 1. The segmentation results obtained by using the new method based on both speed and phase information. There is a substantial improvement in segmentation, especially in the region of the aneurysm (compare Figs. 12(b) and 13(b)). But still, there are some false negative voxels near the singular point. This is because the level of intensity is very low, and the flow pattern is seriously corrupted by noise.

low, and the flow pattern is seriously corrupted by noise. A higher level of understanding of flow topology is required to tackle this problem.

Fig. 25. Patient 2. The segmentation results obtained by using the new method based on both speed and phase information. There is a substantial improvement in segmentation, especially in the region of the aneurysm (compare Figs. 12(b) and 13(b)). But still, there are some false negative voxels near the singular point. This is because the level of intensity is very low, and the flow pattern is seriously corrupted by noise.

4.3. Aneurysm phantom data set

To validate the new segmentation approach, the approach was applied to an in-vitro silicon aneurysm model (middle cerebral artery bifurcation aneurysm: MCA, kindly provided by the Department of Neuroradiology, University Hospital of Geneva, Switzerland). The model was scanned using the PC-MRA protocol on a 1.5 T GE MR scanner as before. The data volume was $256\times256\times23$ voxels with voxel dimensions of $0.8\times0.8\times1$ mm^3. To alleviate the problem of serious motion artifacts induced by the pulsatile motion of the model, it was firmly mounted inside a tailor-made, MR compatible Perspex box completely filled with gelatin. The working fluid was whole blood obtained from expired stocks of the blood bank of The Royal Free Hospital, London. The mean flow rate was set to 300 ml/min for this study (McDonald, 1974).

Figs. 26(a) and (d) show the 3-D reconstruction and a cross-section of the MCA aneurysm respectively, in which the results of segmentation using speed information alone are shown. For the purpose of visualisation, a smooth surface was extracted from the segmented binary images of all slices by using the Visualisation Toolkit (VTK) software package with slight Gaussian smoothing on the surface (standard deviation was set to 1) (Schroeder et al., 1998). A large improvement in segmentation is visually apparent using the new segmentation method, which utilises both speed and phase information, as shown in Figs. 26(b) and (e). The circle in the middle represents regions near singularity of the velocity field, where the flow is extremely low and almost zero. This can be a useful feature to detect because it indicates to the radiologist the position of stagnant flow inside the aneurysm. While it will not greatly affect the quality of visualisation in 3-D because it is lying inside the aneurysmal surface, it will affect any quantitative measure made on the aneurysm. Dealing with such haemodynamic features is an area of ongoing work.

5. Discussion and conclusion

The purpose of this work was to develop fully automatic and accurate vascular segmentation and quantitative analysis methods for magnetic resonance angiography (MRA) to provide patient-specific vascular models that can be used for diagnosis, as well as endovascular treatment (e.g. Guglielmi detectable coils (GDC) method) of aneurysms and other arterial diseases.

We have derived a Maxwell–Gaussian-uniform mixture (MGU) model of the background and vascular signal characteristics of images generated by the phase-difference post-processing algorithm as used in PC-MRA. It has been shown that the MGU model (a) fits better than a Maxwell-uniform (MU) distribution for modelling a PC-MRA image, and (b) gives fewer false positive voxels (mis-

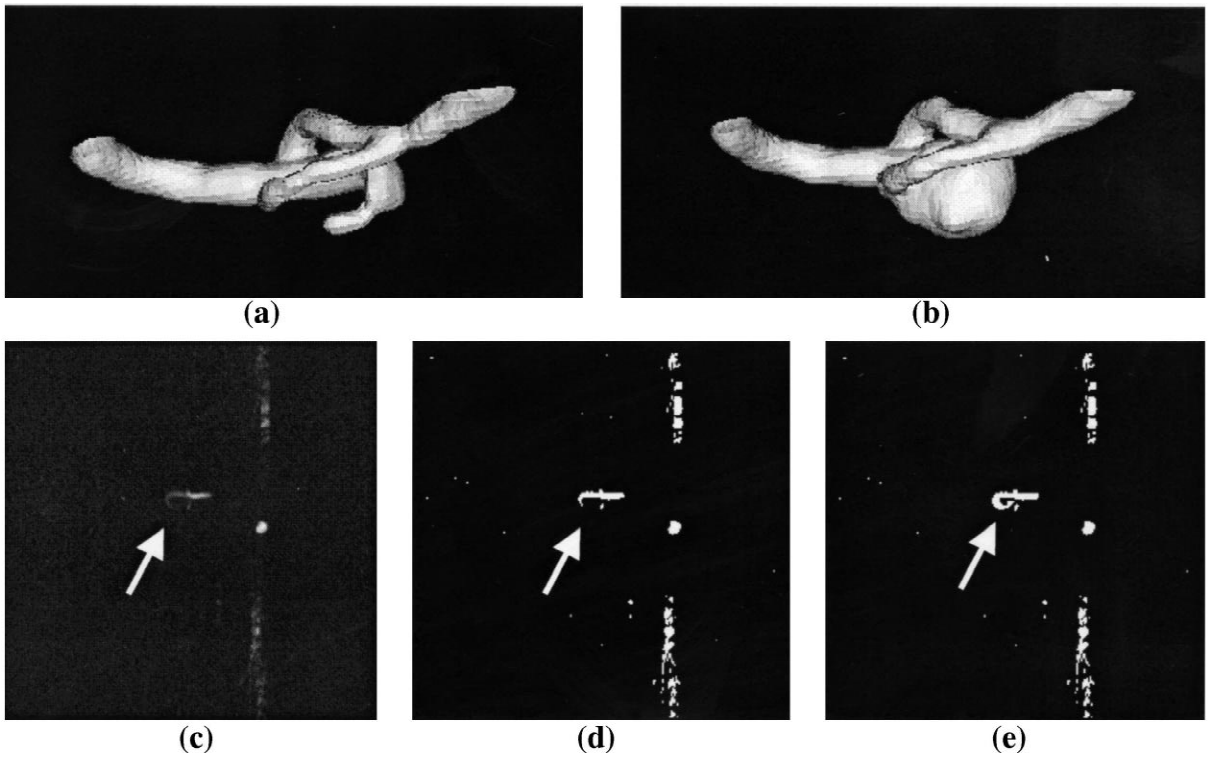

Fig. 26. (a) 3-D reconstruction of the model using speed information alone. (b) 3-D reconstruction of the model using both speed and phase information. (c) Original speed image. (d) Segmented image using speed information alone. (e) Segmented image using both speed and phase information.

classified vessel voxels) in segmentation. Using this mixture model and a local phase coherence (LPC) measure of the velocity field, we have then presented a new statistical approach for aggregating speed and phase information available in PC-MRA data, and demonstrated that inclusion of phase information as a priori knowledge in the MRF model can improve the quality of segmentation, especially in the region within an aneurysm.

In developing the mixture model, we have paid particular attention to the behaviour of the background regions whilst maintaining a relatively simple model of the vascular signals. In practice, the fraction of the image volume attributable to fully resolved vessels (i.e. having diameters $>$voxel dimensions) is around 1–4%. These voxels form the majority of the extended high intensity tail in the frequency histogram of the magnitude-weighted speed images. Given the limited spatial resolution of PC-MRA, a larger number of voxels will contain both static tissue and vessel. A comprehensive model of the distribution of these voxel values, which incorporates partial volume effects, may be possible. However, they will still constitute a small distribution heavily overlapping with that of the much larger background population. The uniform distribution therefore provides a simple estimate of the distribution of fully resolved vessel signals based predominately on the high speed region whilst avoiding some of the errors associated with fitting a small distribution in the presence of comparatively large competing distributions. The use of the LPC measure as a priori knowledge improves the quality of segmentation based on a global threshold of the speed images by adaptively adjusting the local threshold for the extraction of voxels from within the bulk of the background distribution. In this sense, the uniform distribution acts as a conservative bound on the performance of the segmentation in intensity regions below the speed image threshold. Since the freedom afforded by the uniform distribution is less than that we would expect from a full partial volume model, we can anticipate our segmentation is not optimal, but errs on the side of minimising false positives. Nonetheless, the true positive rate is improved over global threshold-based segmentation alone.

In the segmentations performed, it can be observed that ghosts in the image have sometimes been false positively identified as part of the vascular region (e.g. a vertical band in the phantom images). The acquisition of MR images is prone to formation of duplicates of time varying structures (pulsatile vessels) displaced from the true structure in the phase encoding direction(s). The intensity and phase of these ghosts results from coherent superposition of specific harmonics of the spatially encoded data due to modulation of the intensity and phase of the acquired Fourier data. In our results such ghosting was particularly apparent in the phantom data. Variability in the human heart rate and the damped pulsatility of the in-vivo intracranial circulation

may account for this finding. The phase and intensity of the ghosts reflects that of their generating vessel and leaves the segmentation algorithm open to false positive identifications of the ghosts. Measures to reduce ghosting by altering the *k*-space sampling order (McGowan and Wood, 1996) or by auto-focus methods (McGee et al., 2001) have been demonstrated but were not applied to the data herein.

Extension of the technique to three dimensions is straightforward. A possible advantage of doing so is the identification of vessels traversing in the through-plane direction where the additional information from adjacent slices may be incorporated in the LPC measure and the Markov random field framework. Moreover, in related further work, we have investigated the effects of including more in-plane vector pairs in the 2-D LPC measure and the possibility of extending the LPC measure to a higher dimension. The results are published in (Chung, 2001).

The new segmentation method is being used as a vascular segmentation and reconstruction tool in a neuro-interventions planning project, which helps the neuro-radiologist (a) to find the neck plane orientation of the aneurysms and (b) to simulate and select the optimal X-ray projections before the GDC treatments (Wilson et al., 1999). In that application, accurate segmentation and reconstruction of an aneurysm, as well as its surrounding vessels is very important to the success rate and procedural safety of the treatments. Future work will include detection of the flow singular point, which may indicate the presence of an aneurysm, perhaps by using knowledge of flow topology (Helman and Hesselink, 1991) and more detailed studies of the application of the methodology to a large number of aneurysms.

Acknowledgements

The authors would like to thank Prof. J. Byrne and Dr. A. Martinez for giving clinical advice related to this work; Prof. D. Rufenacht and Dr. K. Tokunaga for making the aneurysm model; Ms. J. Blackhall, Dr. T. Lambrou, Mr. K. Rhode and Dr. G. Penney for offering assistance in carrying out the phantom study; and Prof. Michael Brady for giving constructive comments to this paper. A. Chung was funded by a postgraduate scholarship from the Croucher Foundation, Hong Kong.

Appendix A

This appendix shows how the parameters of the Maxwell–Gaussian-uniform (MGU) model can be estimated. Recall from Eq. (9) that, the overall probability density function $f(i)$ of an MRA speed image is given by,

$$f(i) = \underbrace{w_M f_M(i) + w_G f_G(i)}_{\text{Background Signal}} + \underbrace{w_U f_U(i)}_{\text{Vascular Signal}}, \tag{9}$$

where the Maxwell distribution $f_M(i)$ is defined in Eq. (7), the Gaussian distribution $f_G(i)$ is defined as

$$f_G(i) = \frac{1}{\sqrt{2\pi}\sigma_G}\exp\left(\frac{-(i-\mu_G)^2}{2\sigma_G^2}\right), \tag{A.1}$$

and the uniform distribution is defined as $f_U(i) = 1/I_{max}$, where I_{max} is the maximum intensity in the observed frequency histogram of intensities. Given a mixture model of a Maxwell, Gaussian and uniform distributions, there are six parameters: w_M, w_G, w_U, σ_M^2, μ_G and σ_G^2, which need to be estimated.

The modified EM algorithm is an iterative procedure that can be used to estimate the parameters, which maximise the log-likelihood of the mixture distribution at each iteration (Bishop, 1995).

Let the log-likelihood function be $L = \Sigma_{i=0}^{I_{max}} h(i) \log f(i)$, where $h(i)$ is the observed frequency histogram and $f(i)$ is the mixture PDF in Eq. (9). The change in log-likelihood function is given by

$$L^{k+1} - L^k = \sum_{i=0}^{I_{max}} h(i) \log\left(\frac{f^{k+1}(i)}{f^k(i)}\right), \tag{A.2}$$

where index k represents the kth iteration step. We aim to maximise the change of log-likelihood $L^{k+1} - L^k$ until the change is sufficiently small. Suppose that, given an intensity i, the posterior probabilities of the Maxwell, Gaussian and uniform distributions are $P(M|i)$, $P(G|i)$ and $P(U|i)$, respectively. Then $P(M|i) = w_M f_M(i)/f(i)$. The same applies to $P(G|i)$ and $P(U|i)$. Also $P(M|i) + P(G|i) + P(U|i) = 1$. Eq. (A.2) can be rewritten as

$$L^{k+1} - L^k = \sum_{i=0}^{I_{max}} h(i) \log\left(P^k(M|i)\frac{w_M^{k+1} f_M^{k+1}(i)}{f^k(i)P^k(M|i)} + P^k(G|i)\frac{w_G^{k+1} f_G^{k+1}(i)}{f^k(i)P^k(G|i)} + P^k(U|i)\frac{w_U^{k+1} f_U^{k+1}(i)}{f^k(i)P^k(U|i)} \right) \tag{A.3}$$

by expanding $f^{k+1}(i)$ and multiplying $P^k(M|i)$, $P^k(G|i)$ and $P^k(U|i)$ to both numerator and denominator. By Jensen's inequality,

$$\log(\lambda_1 x_1 + \lambda_2 x_2 + \lambda_3 x_3) \geqslant \lambda_1 \log x_1 + \lambda_2 \log x_2 + \lambda_3 \log x_3 \tag{A.4}$$

where $\lambda_1 + \lambda_2 + \lambda_3 = 1$. Let $\lambda_1 = P^k(M|i)$, $\lambda_2 = P^k(G|i)$ and $\lambda_3 = P^k(U|i)$. Then from Eq. (A.3), we have

$$L^{k+1} - L^k \geqslant \sum_{i=0}^{I_{max}} h(i) \left(P^k(M|i) \log\frac{w_M^{k+1} f_M^{k+1}(i)}{f^k(i)P^k(M|i)} + P^k(G|i) \log\frac{w_G^{k+1} f_G^{k+1}(i)}{f^k(i)P^k(G|i)} + P^k(U|i) \log\frac{w_U^{k+1} f_U^{k+1}(i)}{f^k(i)P^k(U|i)} \right). \tag{A.5}$$

Therefore, maximising the right-hand-size of the inequality in Eq. (A.5) is equivalent to ensuring the maximal lower bound to the change in log-likelihood is achieved until the log-likelihood converges to a stationary point (Bishop, 1995).

Maximisation with respect to w_{M}^{k+1}, w_{G}^{k+1} and w_{U}^{k+1}: the right-hand-size of Eq. (A.5) can be rearranged to isolate the terms related to w_{M}^{k+1}, w_{G}^{k+1} and w_{U}^{k+1}. Let

$$Q_w = \sum_{i=0}^{I_{\max}} h(i)\big(P^k(M|i)\log w_{\mathrm{M}}^{k+1} + P^k(G|i)\log w_{\mathrm{G}}^{k+1} + P^k(U|i)\log w_{\mathrm{U}}^{k+1}\big). \tag{A.6}$$

Then we need to maximise Q_w under that constraint $w_{\mathrm{M}}^{k+1} + w_{\mathrm{G}}^{k+1} + w_{\mathrm{U}}^{k+1} = 1$, i.e. maximise $Q_w + \lambda\big(1 - w_{\mathrm{M}}^{k+1} - w_{\mathrm{G}}^{k+1} - w_{\mathrm{U}}^{k+1}\big)$, where λ is the Lagrange multiplier. Setting the derivatives with respect to w_{M}^{k+1}, w_{G}^{k+1} and w_{U}^{k+1} to zero gives

$$\lambda w_{\mathrm{M}}^{k+1} = \sum_{i=0}^{I_{\max}} h(i)P^k(M|i), \qquad \lambda w_{\mathrm{G}}^{k+1} = \sum_{i=0}^{I_{\max}} h(i)P^k(G|i)$$

$$\text{and} \quad \lambda w_{\mathrm{U}}^{k+1} = \sum_{i=0}^{I_{\max}} h(i)P^k(U|i). \tag{A.7}$$

Summing Eq. (A.7) gives $\lambda = N$, where N is the total number of voxels. Hence, we obtain

$$w_{\mathrm{M}}^{k+1} = \frac{1}{N}\sum_{i=0}^{I_{\max}} h(i)P^k(M|i), \quad w_{\mathrm{G}}^{k+1} = \frac{1}{N}\sum_{i=0}^{I_{\max}} h(i)P^k(G|i)$$

$$\text{and} \quad w_{\mathrm{U}}^{k+1} = \frac{1}{N}\sum_{i=0}^{I_{\max}} h(i)P^k(U|i). \tag{A.8}$$

Maximisation with respect to σ_{M}^2: the right-hand side of Eq. (A.5) can be rearranged to isolate the terms related to σ_{M}^2. It gives

$$Q_{\mathrm{M}} = \sum_{i=0}^{I_{\max}} h(i)P^k(M|i)\log f_{\mathrm{M}}^{k+1}(i). \tag{A.9}$$

Setting the derivatives of Q_{M} with respect to σ_{M}^2 to zero gives

$$\sum_{i=0}^{I_{\max}} h(i)P^k(M|i)\big(i^2 - 3\big(\sigma_{\mathrm{M}}^2\big)^{k+1}\big) = 0. \tag{A.10}$$

Therefore, we obtain

$$\big(\sigma_{\mathrm{M}}^2\big)^{k+1} = \frac{\sum_i h(i)P^k(M|i)i^2}{3\sum_i h(i)P^k(M|i)}. \tag{A.11}$$

Maximisation with respect to μ_{G} and σ_{G}^2: the right-hand side of Eq. (A.5) can be rearranged to isolate the terms related to μ_{G} and σ_{G}^2. It gives

$$Q_{\mathrm{G}} = \sum_{i=0}^{I_{\max}} h(i)P^k(G|i)\log f_{\mathrm{G}}^{k+1}(i). \tag{A.12}$$

Setting the derivatives of Q_{G} with respect to μ_G and σ_{G}^2 to zero gives

$$\sum_{i=0}^{I_{\max}} h(i)P^k(G|i)\big(i - \mu_{\mathrm{G}}^{k+1}\big) = 0 \tag{A.13}$$

and

$$\sum_{i=0}^{I_{\max}} h(i)P^k(G|i)\big[\big(i - \mu_{\mathrm{G}}^{k+1}\big)^2 - \big(\sigma_{\mathrm{G}}^2\big)^{k+1}\big] = 0. \tag{A.14}$$

Therefore, we obtain

$$\mu_{\mathrm{G}}^{k+1} = \frac{\sum_i h(i)P^k(G|i)i}{\sum_i h(i)P^k(G|i)}$$

and

$$\big(\sigma_{\mathrm{G}}^2\big)^{k+1} = \frac{\sum_i h(i)P^k(G|i)\big(i - \mu_{\mathrm{G}}^{k+1}\big)^2}{\sum_i h(i)P^k(G|i)}.$$

References

Andersen, A.H., Kirsch, J.E., 1996. Analysis of noise in phase contrast MR imaging. Med. Phys. 23 (6), 857–869.

Atkins, M.S., Mackiewich, B.T., 1998. Fully automatic segmentation of the brain in MRI. IEEE Trans. Med. Imaging 17 (1), 98–107.

Bernstein, M.A., Grgic, M. et al., 1994. Reconstructions of phase contrast, phased array multicoil data. Magn. Reson. Med. 32, 330–334.

Besag, J., 1986. On the statistical analysis of dirty pictures. J. R. Stat. Soc. (B) 48 (3), 259–302.

Bishop, C.M., 1995. Neural Networks for Pattern Recognition. Clarendon Press, Oxford.

Box, G.E.P., Tiao, G.C., 1973. Bayesian Inference in Statistical Analysis. Addison-Welsey, Reading, MA.

Brummer, M.E., Mersereau, R.M. et al., 1993. Automatic detection of brain contours in MRI data sets. IEEE Trans. Med. Imaging 12 (2), 153–166.

Burleson, A.C., Strother, C.M. et al., 1995. Computer modeling of intracranial saccular and lateral aneurysms for the study of their hemodynamics. Neurosurgery 37 (4), 774–784.

Caro, C.G., Pedley, T.J. et al., 1978. The Mechanics of the Circulation. Oxford University Press.

Chung, A.C.S., 2001. Vascular reconstruction for minimally invasive computer-assisted intervention planning. D. Phil. Thesis. University of Oxford.

Chung, A.C.S., Noble, J.A. et al., 2000. Fusing speed and phase information for vascular segmentation in phase contrast MR angiograms. In: Delp, S.L. (Ed.), Proc. Medical Image Computing and Computer-Assisted Intervention, pp. 166–175.

Foutrakis, G.N., Yonas, H. et al., 1999. Saccular aneurysm formation in curved and bifurcating arteries. Am. J. Neuroradiol. 20, 1309–1317.

Frangi, A.F., Niessen, W.J. et al., 1999. Model-based quantitation of 3-D magnetic resonance angiographic images. IEEE Trans. Med. Imaging 18 (10), 946–956.

Geman, S., Geman, D., 1984. Stochastic relaxation, Gibbs distributions, and the Bayesian restoration of images. IEEE Trans. Pattern Anal. Machine Intell. 6 (6), 721–741.

Gobin, Y.P., Counord, J.L. et al., 1994. In vitro study of haemodynamics in a giant saccular aneurysm model. Neuroradiology 36, 530–536.

Gudbjartsson, H., Patz, S., 1995. The Rician distribution of noisy MRI data. Magn. Reson. Med. 34, 910–914.

Held, K., Kops, E.R. et al., 1997. Markov random field segmentation of brain MR images. IEEE Trans. Med. Imaging 16 (6), 878–886.

Helman, J.L., Hesselink, L., 1991. Visualization of vector field topology in fluid flows. IEEE Comp. Graphics Appl. 11 (3), 36–46.

Henkelman, R.M., 1985. Measurement of signal intensities in the presence of noise in MR images. Med. Phys. 12 (2), 232–233.

Kapur, T., Grimson, W.E.L. et al., 1998. Enhanced spatial priors for segmentation of magnetic resonance imagery. In: Wells, W.M. (Ed.), Proc. Medical Image Computing and Computer-Assisted Intervention, pp. 457–468.

Krissian, K., Malandain, G. et al., 1998. Model based multiscale detection and reconstruction of 3D vessels. INRIA-Technical Report 3442, 1998.

Krissian, K., Malandain, G. et al., 1999. Model based detection of tubular structures in 3D images. INRIA-Technical Report 3736, 1999.

Lathi, B.P., 1983. Modern Digital and Analog Communication Systems, Chapter 11. Holt, Rinehart and Winston, New York, London.

Li, S.Z., 1995. Markov Random Field Modeling in Computer Vision. Springer-Verlag, Tokyo.

Lorigo, L.M., Faugeras, O. et al., 1999. Co-dimension 2 geodesic active contours for MRA segmentation. In: Kuba, A. (Ed.), Proc. International Conference on Information Processing in Medical Imaging, pp. 126–139.

Low, M., Perktold, K. et al., 1993. Hemodynamics in rigid and distensible saccular aneurysms: a numerical study of pulsatile flow characteristics. Biorheology 30, 287–298.

Masutani, Y., Schiemann, T. et al., 1998. Vascular shape segmentation and structure extraction using a shape-based region-growing model. In: Dohi, T. (Ed.), Proc. Medical Image Computing and Computer-Assisted Intervention, pp. 1242–1249.

McDonald, D.A., 1974. Blood Flow in Arteries, 2nd Edition. Edward Arnold, London.

McGee, K., Felmlee, J. et al., 2001. Autocorrection of three-dimensional time-of-flight MR angiography of the circle of Willis. Am. J. Roentgenol. 176, 513–518.

McGowan, C., Wood, M., 1996. Phase-encode reordering to minimize errors caused by motion. Magn. Reson. Med. 35, 391–398.

McInerney, T., Terzopoulos, D., 1997. Medical image segmentation using topologically adaptable surface. In: Troccaz, J. (Ed.), Proc. CVRMed-MRCAS'97, (Lecture Notes in Computer Science 1205). Springer-Verlag, Berlin, Germany, pp. 23–32.

Mignotte, M., Collet, C. et al., 1999. Three-class Markovian segmentation of high-resolution sonar images. Comput. Vision Image Understand. 76 (3), 191–204.

Ortega, H.V., 1998. Computer simulation helps predict cerebral aneurysms. J. Med. Eng. Techol. 22 (4), 179–181.

Parzen, E., 1960. Modern Probability Theory and Its Applications. John Wiley & Sons.

Pelc, N.J., Bernstein, M.A. et al., 1991. Encoding strategies for three-direction phase-contrast MR imaging of flow. J. Magn. Reson. Imaging 1, 405–413.

Pappas, T.N., 1992. An adaptive clustering algorithm for image segmentation. IEEE Trans. Signal Processing 40 (4), 901–914.

Rinck, P.A., 1993. Magnetic Resonance in Medicine, 3rd Edition. Blackwell Scientific Publications.

Ripley, B.D., 1991. The use of spatial models as image priors. In: Possolo, A. (Ed.), Spatial Statistics & Imaging Lecture Notes. Monograph Series, Vol. 20. Springer-Verlag, Berlin, Germany, pp. 309–340.

Schroeder, W., Martin, K. et al., 1998. The Visualization Toolkit: An Object-Oriented Approach to 3-D Graphics, 2nd Edition. Prentice Hall, Englewood Cliffs, N.J.

Sethian, J.A., 1999. Level Set Methods and Fast Marching Methods: Evolving Interfaces in Computational Geometry, Fluid Mechanics, Computer Vision, and Materials Science. Cambridge University Press.

Steiger, H.J., Oshinski, J.N. et al., 1997. Computational simulation of turbulent signal loss in 2D time-of-flight magnetic resonance angiograms. Magn. Reson. Med. 37, 609–614.

Strother, C.M., Graves, V.B. et al., 1992. Aneurysm hemodynamics: an experimental study. Am. J. Neuroradiol. 13, 1089–1095.

Summers, P., Bhalerao, A.H. et al., 1997. Multiresolution, model-based segmentation of MR angiograms. J. Magn. Reson. Imaging 7, 950–957.

Verdonck, B., Bloch, I. et al., 1996. Accurate segmentation of blood vessels from 3D medical images. In: Kunt, M. (Ed.). Proc. International Conference on Image Processing, Vol. 3, pp. 311–314.

Westin, C.F., Lorigo, L.M. et al., 2000. Segmentation by adaptive geodesic active contours. In: Delp, S.L. (Ed.), Proc. Medical Image Computing and Computer-Assisted Intervention, pp. 266–275.

Wilcock, D.J., Jaspan, T. et al., 1995. Problems and pitfalls of 3-D TOF magnetic resonance angiography of the intracranial circulation. Clin. Radiol. 50, 526–532.

Wilson, D.L., Noble, J.A., 1999. An adaptive segmentation algorithm for time-of-flight MRA data. IEEE Trans. Med. Imaging 18 (10), 938–945.

Wilson, D.L., Noble, J.A. et al., 1999. Determining X-ray projections for coil treatments of intracranial aneurysms. IEEE Trans. Med. Imaging 18 (10), 973–980.

Wink, O., Niessen, W.J. et al., 2000. Fast delineation and visualization of vessels in 3-D angiographic images. IEEE Trans. Med. Imaging 19 (4), 337–346.

Zhang, Y., Smith, S. et al., 1999. Segmentation of brain MR images using Markov random fields. In: Hawkes, D. (Ed.), Proc. Medical Imaging Understanding and Analysis, pp. 65–68.